

# CMS Draft Analysis Note

*The content of this note is intended for CMS internal use and distribution only*

2012/11/21

Head Id: 153174

Archive Id: 131467:153177M

Archive Date: 2012/10/16

Archive Tag: trunk

## Search for BSM $t\bar{t}$ Production in the Boosted All-Hadronic Final State using pp Collisions at $\sqrt{s} = 8$ TeV

John Conway<sup>1</sup>, James Dolen<sup>3</sup>, Robin Erbacher<sup>1</sup>, Petar Maksimovic<sup>2</sup>, Kevin Nash<sup>2</sup>, Marc Osherson<sup>2</sup>, Justin Pilot<sup>1</sup>, Salvatore Rappoccio<sup>3</sup>, and Ricardo Vasquez-Sierra<sup>1</sup>

<sup>1</sup> University of California, Davis

<sup>2</sup> Johns Hopkins University

<sup>3</sup> SUNY, Buffalo

### Abstract

We present a search for new physics in the form of a massive particle decaying to a pair of top quarks. For large masses, these top quarks will be highly boosted, leading to unique event topologies with merged top decay products. We use jet substructure techniques, including jet pruning and top tagging, to identify these events, and proceed to set limits on the possible cross sections of new physics models. We consider models of RS KK Gluon production as well as generic narrow  $Z'$  resonances. This search represents an update to the existing analysis, using the same tools and methods, with the use of the 8 TeV dataset collected in 2012. We currently use data corresponding to an integrated luminosity of  $11 \text{ fb}^{-1}$ . With this dataset, we exclude RS Gluons with masses up to  $2.1 \text{ TeV}/c^2$ . We also study resonant  $Z'$  models, excluding cross sections of 21 (59) fb, at the 95% CL, for a  $Z'$  model with a mass of 3 TeV and resonance width of 1% (10%).

This box is only visible in draft mode. Please make sure the values below make sense.

PDFAuthor: Justin Pilot  
PDFTitle: Search for BSM  $t\bar{t}$  Production in the Boosted All-Hadronic Final State using  
pp Collisions at 8 TeV  
PDFSubject: CMS  
PDFKeywords: CMS, physics, software, computing

Please also verify that the abstract does not use any user defined symbols

DRAFT

## Contents

1	1	Introduction . . . . .	1
2	2	Analysis Strategy . . . . .	2
3	3	Data Sample . . . . .	3
4	3.1	Trigger Selection . . . . .	3
5	4	Event Selection . . . . .	3
6	4.1	The Top Tagging and W Tagging Algorithms . . . . .	5
7	4.2	Delta-rapidity Cut . . . . .	7
8	4.3	Cleanup Cuts . . . . .	9
9	5	Algorithm Validation . . . . .	11
10	6	Background Estimation . . . . .	14
11	6.1	Simulated Event Samples . . . . .	14
12	6.2	Data-derived Backgrounds . . . . .	15
13	6.3	Closure test of Mass-Modified procedure . . . . .	16
14	7	Event Yields . . . . .	18
15	8	Signal Samples . . . . .	23
16	9	Systematic Uncertainties . . . . .	30
17	9.1	Trigger Efficiency . . . . .	30
18	9.2	Jet Energy Scale . . . . .	30
19	9.3	Jet Energy Resolution . . . . .	30
20	9.4	Jet Angular Resolution . . . . .	30
21	9.5	Substructure Selection Efficiency . . . . .	34
22	9.6	SM $t\bar{t}$ Normalization Uncertainty . . . . .	34
23	9.7	QCD Estimation Uncertainty . . . . .	34
24	10	Statistical Interpretation and Results . . . . .	34
25	10.1	$m_{t\bar{t}}$ Spectrum Enhancement Analysis . . . . .	38
26	11	Conclusion . . . . .	39
27	A	Comparison of 2011 and 2012 datasets . . . . .	41
28	B	2012 Data Pileup Studies . . . . .	41
29	C	Luminosity Dependence of Trigger Selection . . . . .	45

## 1 Introduction

Many models of new physics predict new particles which have enhanced couplings to the third generation of the Standard Model (SM) [1–9]. Thus, the study of the top quark can give important insight into the validity of such models. In the analysis described here, we study top quark pair production to test for the presence of different new physics models. We test for generic models, labeled as  $Z'$ , as well as more specific models, such as RS KK gluon production.

In the high mass ranges accessible by the LHC at  $\sqrt{s} = 8$  TeV, the event topology of  $t\bar{t}$  production requires special techniques. For example  $Z'$  masses of  $\geq 1$  TeV decaying to  $t\bar{t}$ , the produced top quarks will be highly boosted and the subsequent  $t \rightarrow Wb$  decays may merge together. We utilize special reconstruction techniques to identify these boosted top quarks. This analysis searches for  $t\bar{t}$  pairs decaying in the all-hadronic channel. Due to the  $p_T$  range of the boosted top quarks we use differing reconstruction algorithms for identification.

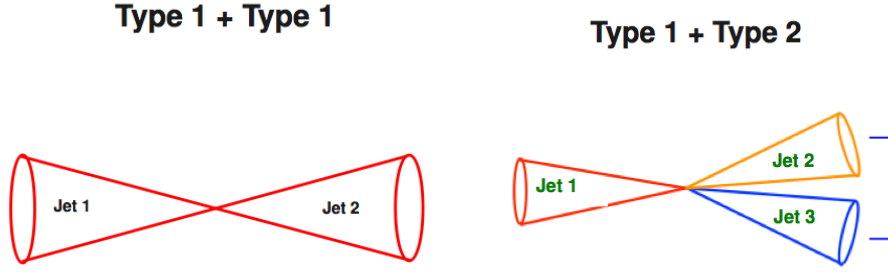


Figure 1: Top quark pair event topologies considered in the analysis.

For moderately-boosted top quarks, the W boson can be reconstructed independently of the b-quark from the top decay. For this topology, we use a jet pruning algorithm to identify the hadronic decay of the W boson, and require a second jet to form the top candidate. For highly-boosted top quarks, all decay products will be merged into a single jet. For this decay topology, we use a special ‘top tagging’ algorithm built on identifying substructure within single jets. We combine these two top decay topologies to search for boosted  $t\bar{t}$  candidate events.

This analysis represents an update to an existing CMS search using the  $\sqrt{s} = 7$  TeV data[10]. We use many of the same techniques and methods to identify candidate events. This analysis is meant to be an expansion of the existing analysis using the 2012  $\sqrt{s} = 8$  TeV CMS dataset. We have studied the effects of the higher center of mass energy on the jet quantities used in the analysis – this can be seen in Appendix A. We also study the effect of the increased number of vertices per bunch crossing. This study can be seen in Appendix B.

## 2 Analysis Strategy

We follow a similar analysis strategy to that described in Ref. [10]. The major changes include the use of an  $H_T$  trigger instead of a single jet trigger, and the use of a control region to verify the data-based background modeling. Additionally, we have increased the leading jet  $p_T$  cut from 350 to 400 GeV/ $c$ , motivated by the change in trigger selection.

We still utilize the same two event topologies considered in the previous analysis. ‘Type 1’ top candidates consist of a single jet where all the decay products (the quarks from the W boson decay and the b quark) merge into a single jet. ‘Type 2’ top candidates are partially merged, consisting of a single jet encompassing the decays of the W boson, and an additional jet corresponding to the b quark. The signal region for this region includes only the ‘type 1+1’ topology. We use the ‘type 1+2’ topology as a control region to test our data-based background estimation procedure. The sensitivity of the type 1+2 channel is approximately an order of magnitude less than that of the 1+1 channel, so removing it from the signal region will not affect the overall sensitivity of the analysis. The ‘type 2+2’ events, along with top candidates where all decay products correspond to separate jets, are not selected in this analysis, due to the desire to be in the boosted regime described above. Figure 1 shows the two event topologies utilized in this analysis.

The final state of this signature consists of several high- $p_T$  jets, therefore the largest background will be QCD multijet production. This background is estimated using a data-derived method

Dataset	Luminosity
/Jet/Run2012A-13Jul2012-v1/AOD	803 pb <sup>-1</sup>
/JetHT/Run2012B-13Jul2012-v1/AOD	4387 pb <sup>-1</sup>
/JetHT/Run2012C-PromptReco-v1/AOD	491 pb <sup>-1</sup>
/JetHT/Run2012C-PromptReco-v2/AOD	5308 pb <sup>-1</sup>
<b>Total Integrated Luminosity</b>	<b>10.989 fb<sup>-1</sup></b>

Table 1: Primary datasets used in this analysis, including the corresponding integrated luminosity of each dataset.

described in a following section. In addition to the QCD multijet background, we consider SM  $t\bar{t}$  production using simulated events. After validating our model of the data, we proceed to test for the presence of a signal due to several new physics model hypotheses.

### 3 Data Sample

We use data collected during the 2012 LHC run with collisions at  $\sqrt{s} = 8$  TeV. Table 1 summarizes the datasets used for this analysis, along with the corresponding integrated luminosity. Currently we are using data corresponding to an integrated luminosity of approximately 11 fb<sup>-1</sup>.

#### 3.1 Trigger Selection

During the 2012 LHC running, a different set of triggers is in use compared to the 2011 run. This affects the choice of triggers used in this analysis. The previous analysis in this channel used the trigger `HLT_Jet300`, which selected events using CaloJets. For this analysis, we use the `HLT_HT750` trigger – this is the lowest un-prescaled  $H_T$  trigger present in the 2012 trigger menus.<sup>1</sup> We measure the trigger efficiency by emulating this trigger in the signal and  $t\bar{t}$  Monte Carlo samples, using the standard HLT tools. As the  $H_T$  trigger uses the summed energy of all the objects in the event, we parameterize the trigger efficiency using the sum of the  $p_T$  of all reconstructed jets present in the event considered for offline analysis. Figure 2 shows the trigger efficiency curve obtained, parameterized as a function of the sum jet  $p_T$ . The trigger efficiencies obtained here are applied to the Monte Carlo samples used in the analysis. A separate trigger efficiency curve is used for the type 1+1 and type 1+2 channels. These curves are measured using the full selection for each channel, as described below.

### 4 Event Selection

We use the same event selection as in [10], with the main change being an increase in the leading jet  $p_T$  cut to 400 GeV/ $c$  instead of 350 GeV/ $c$ .

All data are reconstructed using CMSSW 5.3.x, using the global tag `GR_P_V40_AN1`. Event data are reconstructed using the particle-flow reconstruction algorithm [11], which attempts to reconstruct all stable particles in an event by combining information from all subdetectors. The algorithm categorizes all particles into five types: muons, electrons, photons, charged and neutral hadrons. The resulting particle flow candidates are passed to each jet clustering algorithm to create “particle flow jets”, in this case the Cambridge-Aachen (CA) jet clustering algo-

<sup>1</sup>We also considered the use of the trigger `HLT_PFJet320`, but observed some luminosity-dependent effects that affect the background modeling in the analysis. Further information on these effects can be found in Appendix C.

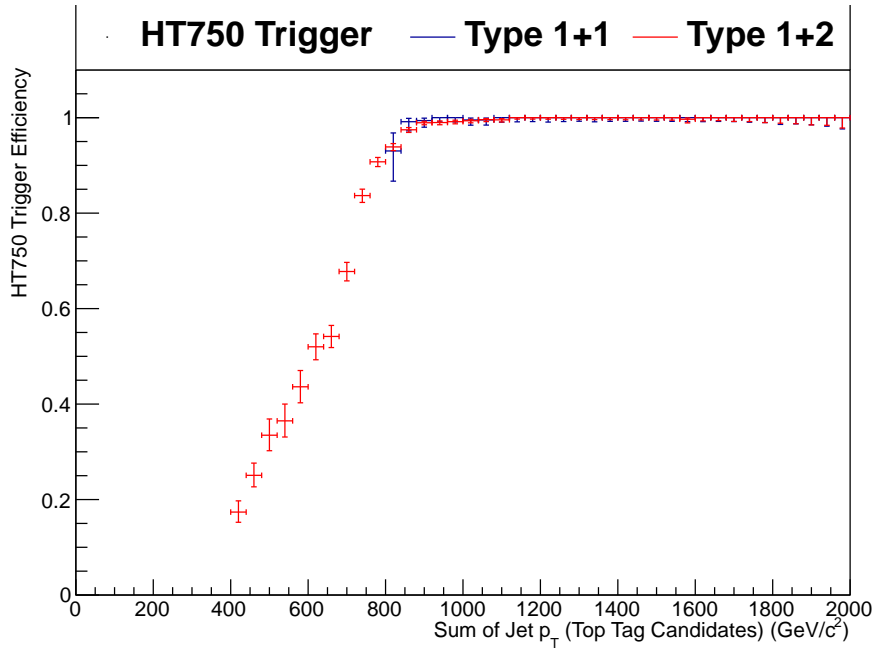


Figure 2: Trigger efficiency for the `HLT_HT750` trigger, parameterized as a function of the sum of the  $p_T$  of all jets. These curves are obtained by using the trigger emulation on the RS Gluon signal samples listed in Table 4.

rithm [12, 13], as implemented in FastJet version 3 [14]. The CA clustering sequence is only determined by the distance between clusters and is not weighted by their momentum, as is done for the  $k_T$  and anti- $k_T$  algorithms. A distance parameter of size  $R = \sqrt{(\Delta\eta)^2 + (\Delta\phi)^2} = 0.8$  is used. In previous studies based on simulation [15], the CA algorithm was found to be more efficient (for the same mistag rate) than  $k_T$  or anti- $k_T$  at finding hard subjets when the clustering sequence is reversed [15].

Charged hadrons identified as pileup are removed from the inputs to the jet clustering algorithms. The charged hadrons are classified as belonging to a pileup vertex when they are used to reconstruct a vertex that is not the highest  $p_T$  primary vertex. Furthermore, charged leptons with an isolation of 15% (muons) or 20% (electrons) of the lepton transverse momentum are also removed, where the isolation is defined as the fraction of energy from charged particles, neutral particles, and photons (counted separately).

After these subtractions, only the neutral component of pileup remains; it is removed by applying a residual area-based correction as described in Ref. [16, 17]. The mean  $p_T$  per unit area is computed with the  $k_T$  algorithm with the “active area” method, with a distance parameter of 0.6, and the jet energy is corrected by the amount of pileup expected in the jet area. The “active area” method adds a large number of infinitely soft “ghost” particles to the clustering sequence to examine which jet they are clustered into, and the area is computed by the set of points for each jet.  $\eta$ -dependent jet corrections are also necessary, due to the different responses in the endcap and barrel calorimeters. The amount of energy expected from underlying event is added back into the jet. The pileup-subtracted jet four momenta are finally corrected for nonlinearities in  $\eta$  and  $p_T$  with simulated data, with a residual  $\eta$ -dependent correction added to correct for the difference in simulated and true responses [18]. Constituents of the jet (i.e. subjets) are not corrected, and algorithmic procedures are done on uncorrected jet energies.

The corrections for the CA  $R = 0.8$  jets are derived from studies using the anti- $k_T$   $R = 0.5$

jet algorithm. Simulation studies confirm [10] that these anti- $k_T$ -derived jet corrections are adequate for the CA  $R = 0.8$  jet algorithm for the jet momenta considered here. We use the 2012 prescription for jet energy corrections[19], which is taken from the first  $\sim 1.6 \text{ fb}^{-1}$  of integrated luminosity. A further description of additional jet energy corrections due to using jet substructure techniques is described below.

The following preselection is applied.

- The event must have a good primary vertex as computed by a deterministic annealing filter (DAF) ( $|z_{\text{Primary Vertex}}| < 24 \text{ cm}$ ,  $N_{\text{DOF}} > 6$ ).
- The “type 1 + 1” events are required to have at least two jets with
  - $p_T > 400 \text{ GeV}/c$ ,  $|y| < 2.5$
  - Loose particle flow jet identification [20] is applied
- The “type 1 + 2” events are required to have at least three jets with
  - Leading jet constructed with the top tagging algorithm:  $p_T > 400 \text{ GeV}/c$ ,  $|y| < 2.5$
  - Second jet constructed with the jet pruning algorithm:  $p_T > 200 \text{ GeV}/c$ ,  $|y| < 2.5$
  - Third jet constructed with the jet pruning algorithm:  $p_T > 30 \text{ GeV}/c$ ,  $|y| < 2.5$
  - Loose particle flow jet identification [20] is applied
- Beam background events are removed using the following requirements:
  - In events with at least 10 tracks, a minimum of 25% of these tracks must be high purity tracks.

#### 4.1 The Top Tagging and W Tagging Algorithms

The products of hadronic decays of top quarks or  $W$  bosons can fall within a single jet if these particles are boosted relative to their mass. The top and  $W$  tagging algorithms are developed to identify these boosted top and  $W$  jets [21].

Figure 3 shows the efficiency of the top tagging and  $W$  tagging algorithms, using a  $\sqrt{s} = 8 \text{ TeV}$  simulated  $Z' \rightarrow t\bar{t}$  sample. Because jet masses increase with  $p_T$ , the efficiency falls off at high  $p_T$  as jets no longer satisfy the mass window requirements. Even so, for jets with  $p_T$  of roughly 600 to 800  $\text{GeV}/c$ , the expected top tagging efficiency is greater than 50%.

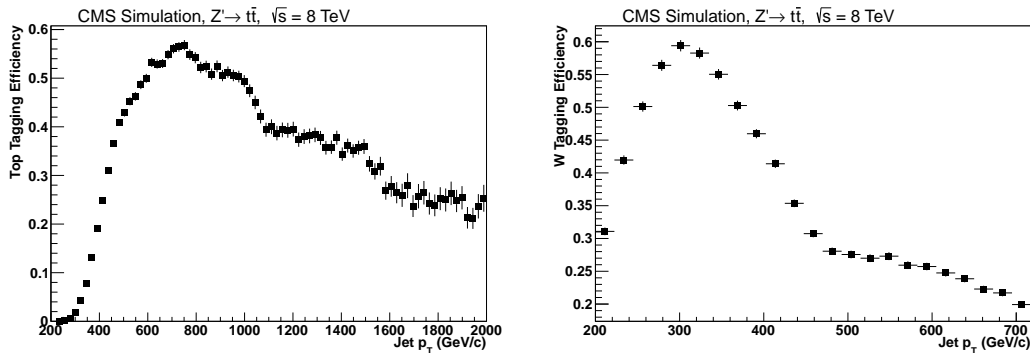


Figure 3: Expected efficiency of the top (left) and  $W$  (right) tagging algorithms derived using simulated  $Z' \rightarrow t\bar{t}$  events.



### 4.1.1 Top Tagging Algorithm

In the top tagging algorithm, Cambridge-Aachen  $R = 0.8$  jets are used as inputs (where  $R = \sqrt{\Delta\eta^2 + \Delta\phi^2}$ ), as described in Section 4. The input CA jets are hereby referred to as the “hard jets.” The algorithm has two steps: the primary decomposition, in which the algorithm attempts to split the hard jet into two subjets, and the secondary decomposition, in which the algorithm attempts to split the subjets found by the primary decomposition. In the process, soft and wide-angle particles (relative to the parent in the clustering) are ignored. At least three subjets are required. The following variables, defined for each jet passing the algorithm, are used to tag top jets:

- **Jet Mass  $m_{\text{jet}}$**  - The mass of the four-vector sum of the constituents of the hard jet.
- **Number of Subjets  $N_{\text{subjets}}$**  - The number of subjets found by the algorithm.
- **Minimum Pairwise Mass  $m_{\text{min}}$**  - The three highest  $p_T$  subjets are taken pairwise, and each pair’s invariant mass is calculated via  $m_{ij} = \sqrt{(E_i + E_j)^2 - (\vec{p}_i + \vec{p}_j)^2}$ .  $m_{\text{min}}$  is the mass of the pair with the lowest invariant mass ( $m_{\text{min}} = \min[m_{12}, m_{13}, m_{23}]$ ). This variable is not defined for jets with less than three subjets.

Jets that have mass close to the top mass, at least three subjets, and minimum pairwise mass close to the  $W$  mass are tagged as top jets. These cuts are designed after the JHU Top Tagging algorithm described in Ref. [22]. Specifically:

$$140 < m_{\text{jet}} < 250 \text{ GeV}/c^2 \quad (1)$$

$$N_{\text{subjets}} \geq 3 \quad (2)$$

$$m_{\text{min}} > 50 \text{ GeV}/c^2 \quad (3)$$

### 4.1.2 W tagging algorithm

The jet pruning algorithm also uses the Cambridge-Aachen  $R = 0.8$  jets as inputs, described in Section 4. In contrast to the top tagging algorithm, the jet pruning algorithm reclusters the jet starting from the constituents, but again removes soft and wide-angle clusters. The same parameters are chosen for the jet pruning algorithm as in the original theoretical papers [23, 24]. The following selection is also applied, which exploits the variables used in Ref. [25]:

- **Number of Subjets  $N_{\text{subjets}}$**  - Require two subjets in the pruning algorithm.
- **Pruned Jet Mass  $m_{\text{jet}}$**  - Require the total pruned jet mass to satisfy  $60 \text{ GeV}/c^2 < m_{\text{jet}} < 130 \text{ GeV}/c^2$ .
- **Mass Drop** - To calculate the mass drop variable, one needs to reverse the last clustering iteration where two components are merged to form the pruned jet. These two components are the two subjets of the pruned jet (one can require different numbers of subjets by continuing to reverse steps in the clustering sequence). These two subjets are then sorted by mass, with the more massive subjet ( $m_1$ ) being used to calculate the mass drop of the pruned jet,  $\mu = \frac{m_1}{m_{\text{jet}}}$ . The mass drop  $\mu$  is required to be less than 0.4 in the  $W$  tagging algorithm. The mass drop requirement ensures that the mass of the jet is roughly evenly spread between two or more subjets. This is the case for heavy particle decays, where QCD jets generally have a hard central core with a very soft additional subjet leading to a high mass drop value.

These criteria are designed to select  $W$  candidates in which the daughter subjets are similar in energy and mass.



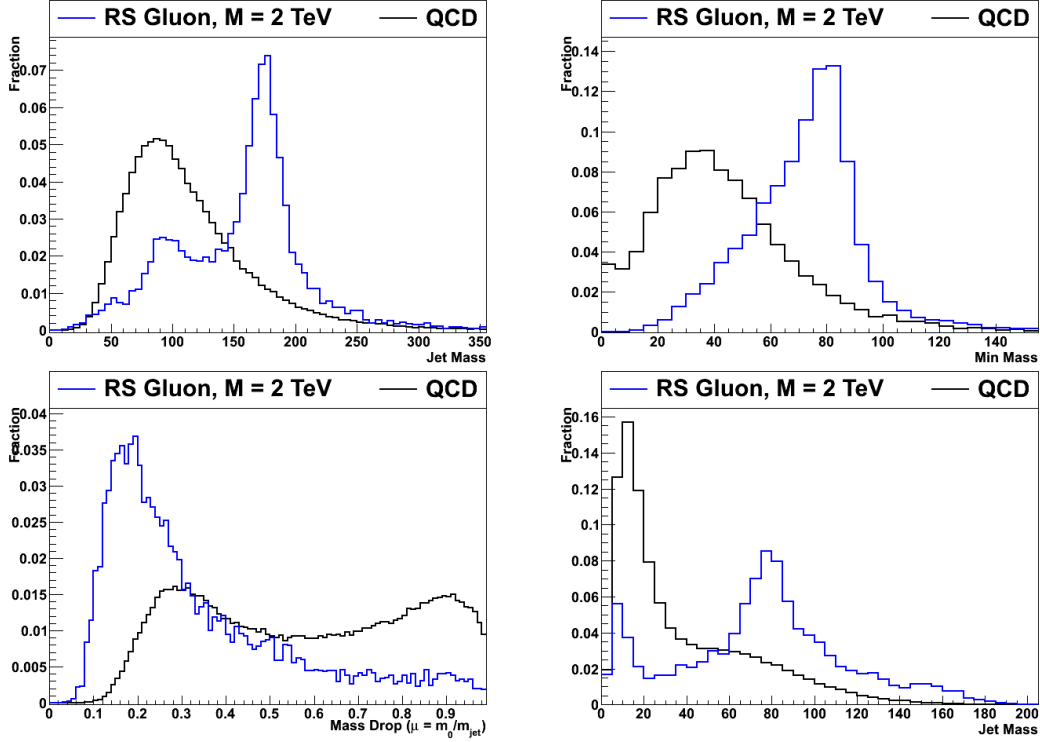


Figure 4: Comparison of some jet substructure quantities for an RS Gluon sample (blue) and a QCD Monte Carlo sample (black), with center-of-mass energies equal to 8 TeV. The jet substructure variables have good discriminating power. Here, the RS Gluons decay to  $t\bar{t}$ .

Figure 4 shows a comparison of these substructure quantities between the RS Gluon sample ( $m = 2 \text{ TeV}/c^2$ ) and a QCD Monte Carlo sample, both for  $\sqrt{s} = 8 \text{ TeV}$ . The discriminating power can be seen in these substructure variables. We also show these distributions with all cuts applied, except for the cut on the variable being plotted. In this way, the added discriminating power of each variable can be seen more clearly. These distributions are shown in Figure 5.

An extensive study of the kinematic distributions of the top and  $W$  taggers has been performed in Ref. [21]. The main conclusions from that public study were that the primary effect of the shapes of QCD jets was from the parton shower and underlying event model, with secondary importance due to pileup.

One consequence of the increased jet  $p_T$  cut (from 350 to 400  $\text{GeV}/c$ ) is the effect on the mass distributions. The jet  $p_T$  and jet mass are highly correlated, so we see a general increase in the jet mass distribution in this version of the analysis. Figure 6 shows the correlation between jet  $p_T$  and jet mass, for a sample of jets from QCD Monte Carlo simulation.

## 4.2 Delta-rapidity Cut

To further enhance the sensitivity of this analysis, we implement a cut on the difference in rapidity ( $\Delta y$ ) between the two top-tagged jets in type 1+1 events. For high values of  $m_{t\bar{t}}$ , jets from a massive particle decay will be closer together, while QCD events will have jets that are more separated to give the high invariant top pair mass. Figure 7 shows a comparison of the  $\Delta y$  distributions for a signal sample (3 TeV  $Z'$ , 1% width) and QCD sample. The effect only becomes significant for high  $m_{t\bar{t}}$ .

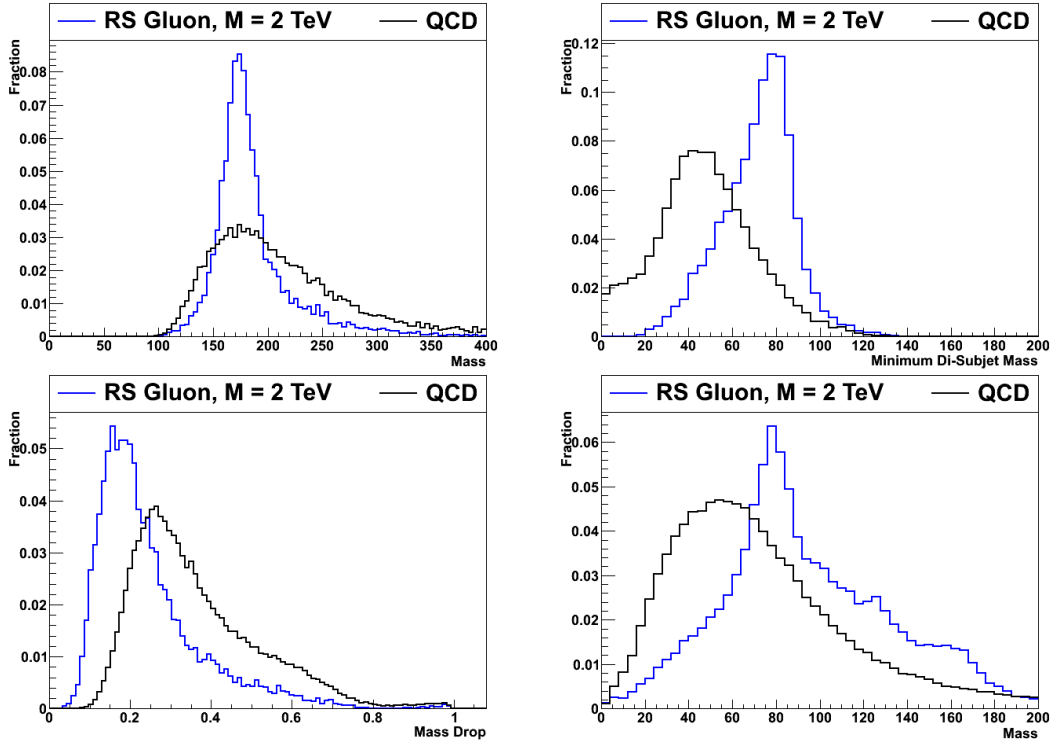


Figure 5: Comparison of jet substructure quantities for an RS Gluon sample (blue) and a QCD Monte Carlo sample (black), with all substructure cuts applied, except for the cut on the variable being plotted. The top row shows substructure quantities for the top tagging algorithm, while the bottom row shows quantities for the W tagging algorithm. Here, the RS Gluons decay to  $t\bar{t}$ . Both samples have center-of-mass energies equal to 8 TeV.

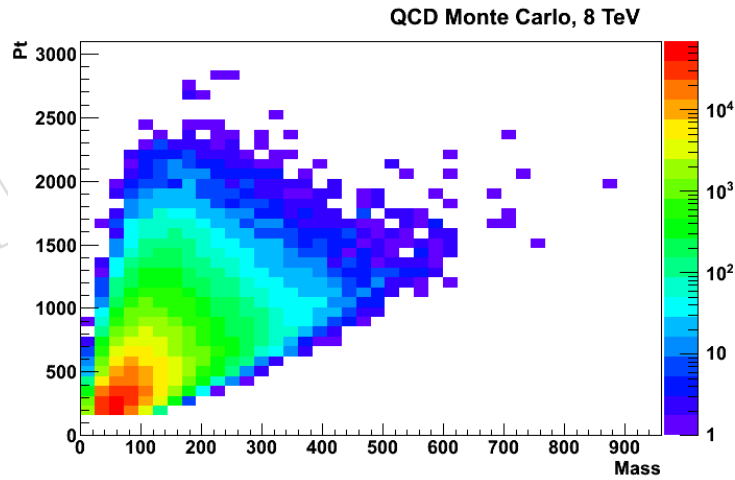


Figure 6: Correlation plot of jet  $p_T$  against jet mass, for a sample of QCD jets from Monte Carlo simulation. Increasing the jet  $p_T$  cut in the analysis has the effect of shifting the jet mass distribution to higher values.

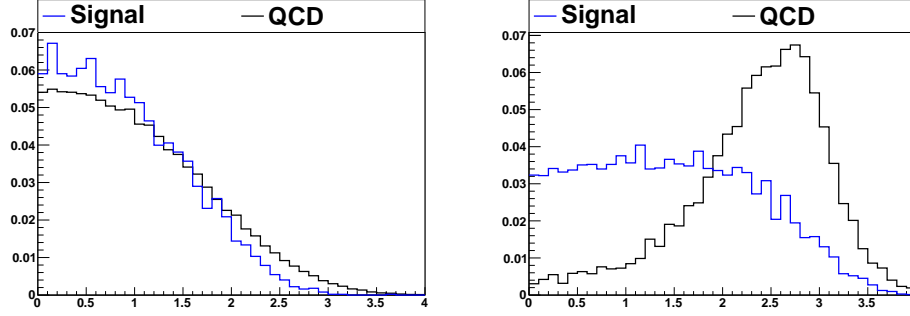


Figure 7: Plots of the  $\Delta y$  distribution for a 3 TeV narrow  $Z'$  signal (blue) and QCD (black) events. For high values of  $m_{\tilde{t}\bar{t}}$ , the signal falls at low values of  $\Delta Y$ , while the QCD background is generally higher.

We optimize this cut by looking at the cumulative integral of signal and background events passing a proposed cut on  $\Delta y$ . We then calculate the ratio  $S/\sqrt{B}$ , where  $S$  represents the number of signal events and  $B$  the number of background events. This optimization is done in the high-mass region,  $m_{\tilde{t}\bar{t}} > 2$  TeV. Figure 8 shows this plot for the 3 TeV RS Gluon signal optimization. We choose to use the same cut for each signal mass point, instead of performing this optimization independently for each signal hypothesis. The differences were observed to be on the order of approximately 0.1 in the optimal value of  $\Delta y$  for each signal hypothesis.

### 4.3 Cleanup Cuts

In previous versions of this analysis, an excess was observed in the final type 1+1  $m_{\tilde{t}\bar{t}}$  distribution. These events are due to a failure of the jet reconstruction due to tracking software. This failure causes many fake tracks to be reconstructed and assigned to the jet, leading to a large number of jet constituents. Because this analysis is sensitive to substructure information and the way the background estimate is determined from data, we are sensitive to these events with tracking failures. A prescription is available from the tracking group, and we plan to implement that event filter. In this version of the analysis note, we make a simple cut to eliminate a large fraction of these events.

The tracking failures only occur in the transition region between the barrel and end-cap regions of the detector,  $1.0 < |\eta| < 1.5$ . Figure 9 shows a two-dimensional plot of the ratio of the charged component of the jet energy to the neutral component of the jet energy, against the  $\eta$  coordinate of the jet. Because of the large number of fake tracks, the charged energy component is expected to be inflated, leading to large values of the charged-to-neutral energy ratio ( $R_{CN}$ ). This is seen as the spike in Figure 9, corresponding to the affected  $\eta$  ranges. This plot is made with a sample of events in which the tracking failure problem occurs.

For this version of the analysis, we choose to place a cut on  $R_{CN} > 2.0$ , only for jets which fall in the affected  $\eta$  range of  $1.0 < |\eta| < 1.5$ . This cut has an efficiency of 90-93% depending on the signal mass point, and removes approximately 95% of the events in a test sample enriched in events with tracking failures.

## 5 Algorithm Validation

To apply the top tagging and W tagging algorithms, it is necessary to measure several quantities that affect jet kinematics. These include the subjet energy scale, and the selection efficiency of

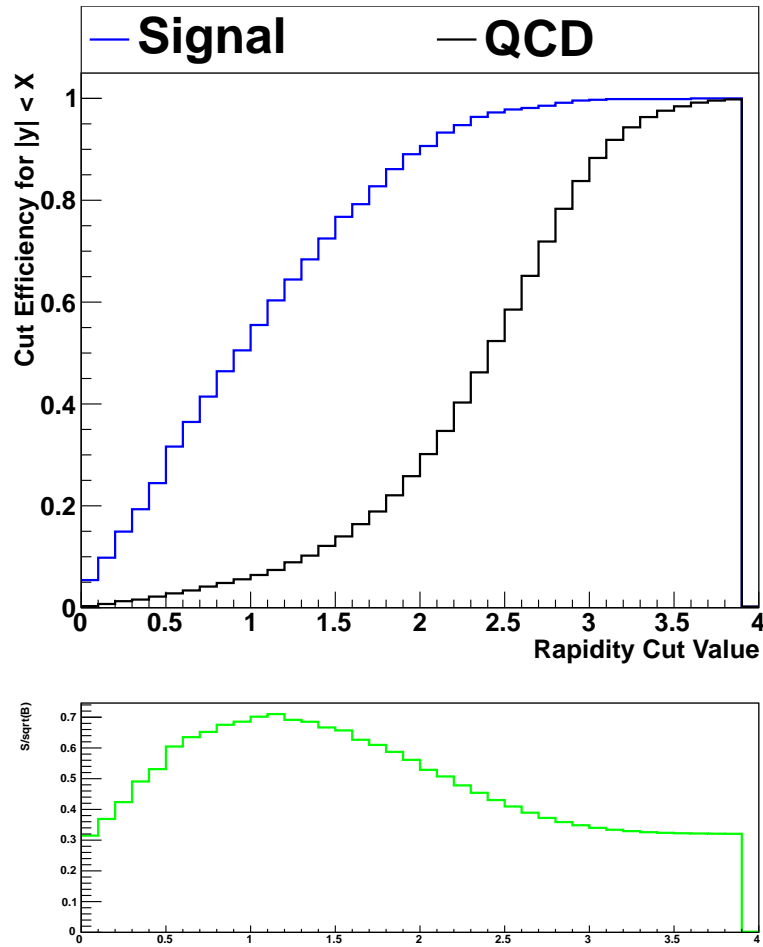


Figure 8: Plots of the  $\Delta y$  distribution for a 3 TeV narrow  $Z'$  signal (blue) and QCD (black) events. For high values of  $m_{t\bar{t}}$ , the signal falls at low values of  $\Delta Y$ , while the QCD background is generally higher.

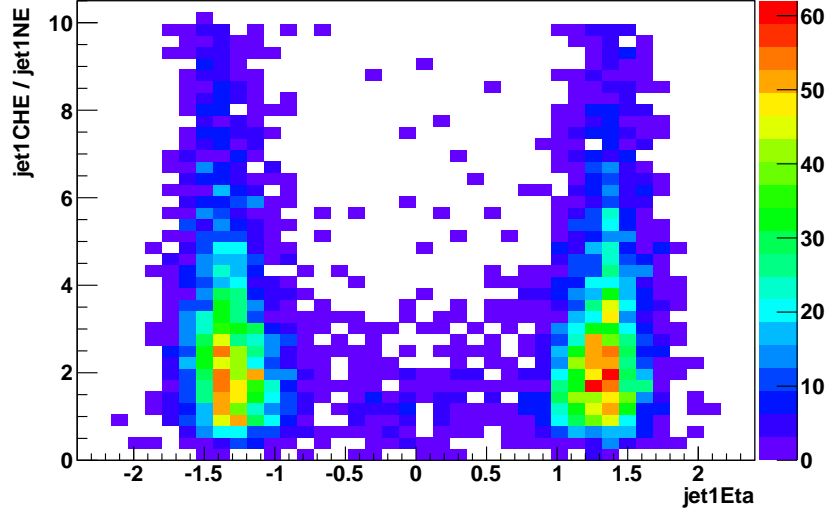


Figure 9: Two-dimensional plot of the charged-to-neutral energy ratio against the  $\eta$  coordinate of the leading jet in the event. Events with the tracking failures have high values of this ratio in the affected range  $1.0 < |\eta| < 1.5$ .

the cuts on substructure quantities.

We follow the same procedure described in Ref. [10] to measure these factors. A muon+jets semileptonic  $t\bar{t}$  sample is used, with the hadronic top candidate being used for the measurements. The event selection for the muon+jets sample is as follows:

- Tight Muon Selection

- $p_T > 45 \text{ GeV}/c$
- $|\eta| < 2.1$
- Not contained in a sub-leading primary vertex
- `isTracker()` and `isGlobalMuon()`
- $\chi^2/N_{DOF} < 10$
- $N_{TrackerHits} > 10$
- $N_{PixelHits} > 0$
- $N_{MuonHits} > 0$
- $d_0 < 0.02 \text{ cm}$  (with respect to the hardest DAF PV)
- $I_{rel} < 0.12$  (using a cone size of  $R = 0.4$ )
- Number of matched stations  $> 0$
- no other isolated muons are allowed

- Loose Muon Selection

- $p_T > 45 \text{ GeV}/c$
- Not contained in a sub-leading primary vertex
- $I_{rel} < 0.20$

The jet selection is similar to that of the type 1+2 channel: two or more jets are required, with  $p_T > 30 \text{ GeV}/c$ . The leading jet is required to have  $p_T > 200 \text{ GeV}/c$ , and also is required to pass the mass drop criteria  $\mu < 0.25$ . Events are divided into two hemispheres based on the position

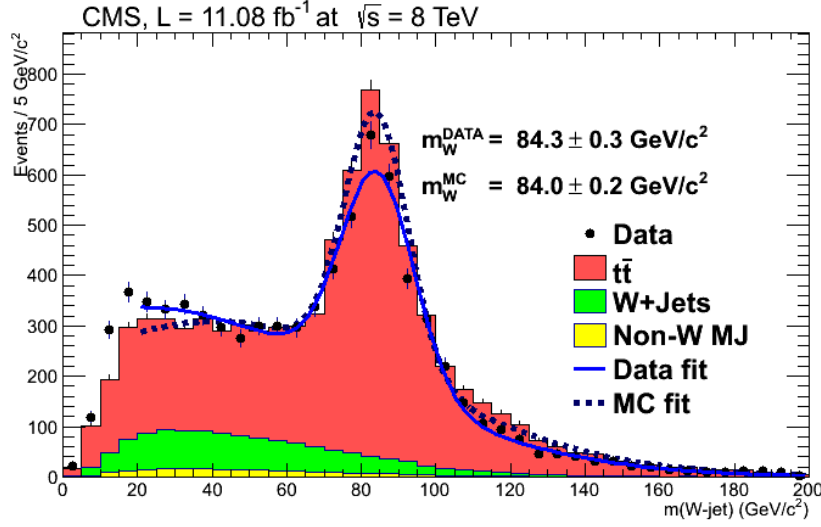


Figure 10: Highest jet mass in the hemisphere opposite the identified muon. A fit is performed to extract the W mass in the data and Monte Carlo distributions.

of the lepton. The jet passing the mass drop criteria must be in the hadronic hemisphere of the event. We require one jet in the event to have a b-tag, using the combined secondary vertex (CSV) tagger at the ‘medium’ operating point (CSVM, where a tagged jet has a value larger than 0.679). The b-tagged jet is not required to combine with the W candidate jet – we only require the presence of the b-tagged jet, and form the hadronic top candidate by combining the W candidate jet with the nearest jet in the corresponding hemisphere that satisfies the event selection.

We apply the above selection to the `SingleMu` primary dataset, using the trigger `HLT_IsoMu40_eta2p1`. We also utilize a W+jets and  $t\bar{t}$  Monte Carlo sample for this measurement. To model the small but non-negligible QCD background, we select a sample of events using the loose muon selection described above. The QCD background normalization is derived from a fit to the  $H_T \equiv E_T^{\text{miss}} + p_T^\mu$  spectrum. The  $H_T$  spectrum is formed from events prior to any mass or substructure selection has been applied to produce the scale factor and efficiency numbers quoted below. The fit determines the relative proportions of the  $t\bar{t}$ , W+jets, and QCD events which make up this sample. These fractions are then used to normalize the templates after the full mass and substructure selections have been applied. The shape of the W+jets contribution is used for the QCD estimate, with the normalization taken from the fit described above.

After performing the fit to the  $H_T$  spectrum to determine the QCD normalization, we plot the highest jet mass in the hemisphere opposite that containing the lepton. We expect to find hadronic W jets in this hemisphere, since this sample consists mainly of semileptonic  $t\bar{t}$  events. A fit is performed to the sum of two Gaussian distributions, for both the data and the total background distributions. The values of  $m_W$  in each case are determined from the fit, and the ratio of the values in data and Monte Carlo is the subjet energy scale factor. Figure 10 shows the jet mass distribution, with the fits to data and Monte Carlo. We measure a value of  $m_W = 84.35 \pm 0.35 \text{ GeV}/c^2$  in the data, and a value of  $m_W = 84.0 \pm 0.2 \text{ GeV}/c^2$  in the Monte Carlo. This results in a value of  $1.004 \pm 0.005$  for the subjet energy scale factor.

The semileptonic sample is also used to determine the efficiency of the mass drop ( $\mu$ ) cut used in the jet pruning algorithm. Figure 11 shows the mass drop distribution in this sample. The

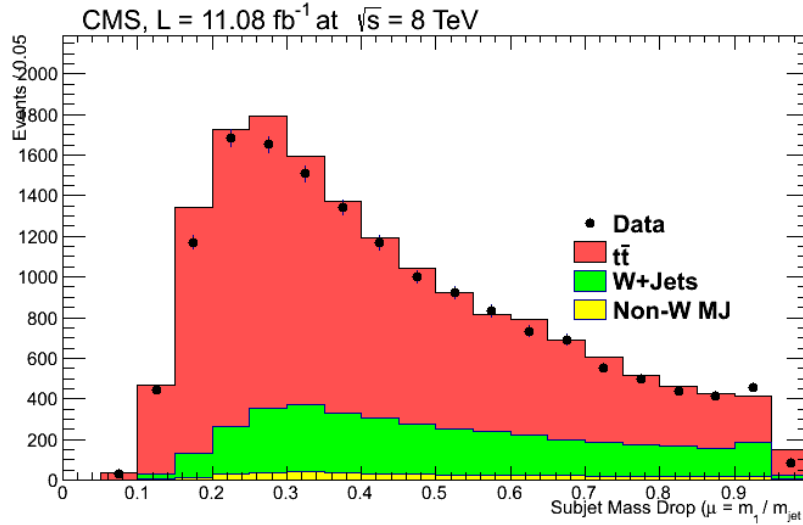


Figure 11: Mass drop ( $\mu$ ) distribution for the semileptonic sample. The difference in efficiencies for a cut of  $\mu < 0.4$  gives the scale factor used in the all-hadronic analysis.

efficiency scale factor is extracted from this sample by evaluating the difference in efficiencies for a cut of  $\mu < 0.4$  in the data and Monte Carlo distributions. We measure an efficiency of  $57.6 \pm 0.4\%$  in the data, and  $58.3 \pm 0.4\%$  in the Monte Carlo for a cut of  $\mu < 0.4$ . This gives a scale factor of  $0.98 \pm 0.009$ .

We also form type 2 top candidates in the semileptonic sample by combining the jets in Figure 10 with an additional (closest) jet in the same hemisphere. This attempts to merge the hadronic W jet with the b-quark jet from the top decay. Although we have required a b-tag in the event to reduce backgrounds, we use only the nearest jet to the hadronic W candidate, which is not required to have a b-tag. For this selection, the leading jet mass is required to be in the window  $[60, 130] \text{ GeV}/c^2$ . Figure 12 shows the distribution obtained with this procedure. Again we measure a scale factor for this mass cut. With efficiencies of  $48.2 \pm 0.6\%$  for data, and  $51.0 \pm 0.6\%$  for Monte Carlo, we obtain a scale factor of  $0.945 \pm 0.015$ . The scale factors for the mass drop cut and the mass window cut are combined to obtain a total scale factor of  $0.935 \pm 0.017$ . This value is used in the analysis on top and W tagged jets.

Additionally, we look for events containing a fully merged (type 1) top candidate in the muon+jets selection. Figure 13 shows the mass distribution of the leading jet in the hadronic hemisphere passing the top-tagging requirements.

## 6 Background Estimation

This analysis has two sources of background: QCD multijet events, determined from data, and SM  $t\bar{t}$  events, determined from simulated events. This section describes the methods for estimating the various background contributions.

### 6.1 Simulated Event Samples

We use a sample of simulated events to estimate our background from SM continuum  $t\bar{t}$  events. This high-statistics ( $\sim 5.2$  million events) sample was generated with Powheg, and we use a cross section of  $\sigma_{t\bar{t}} = 225 \text{ pb}$  for normalization to determine the expected number of events.



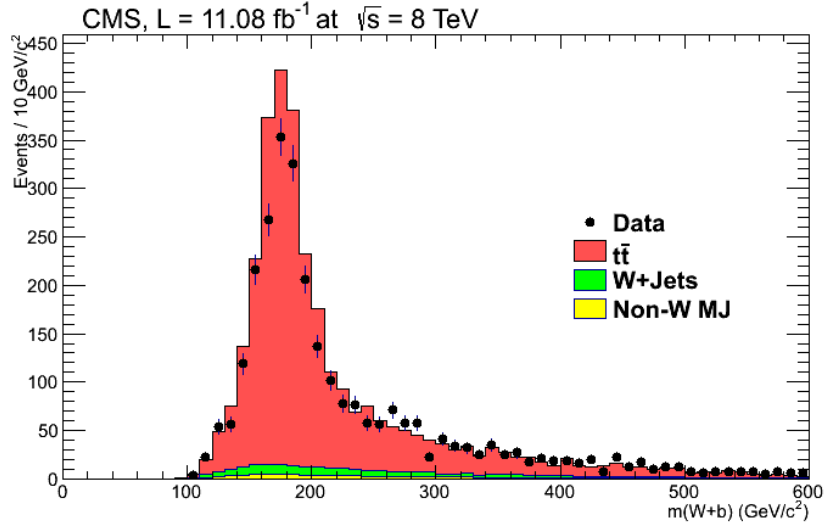


Figure 12: Mass of type 2 top candidates formed in the semileptonic sample by combining jets in the hemisphere opposite that of the lepton. The leading jet is required to have a mass in the range  $[60, 130] \text{ GeV}/c^2$ .

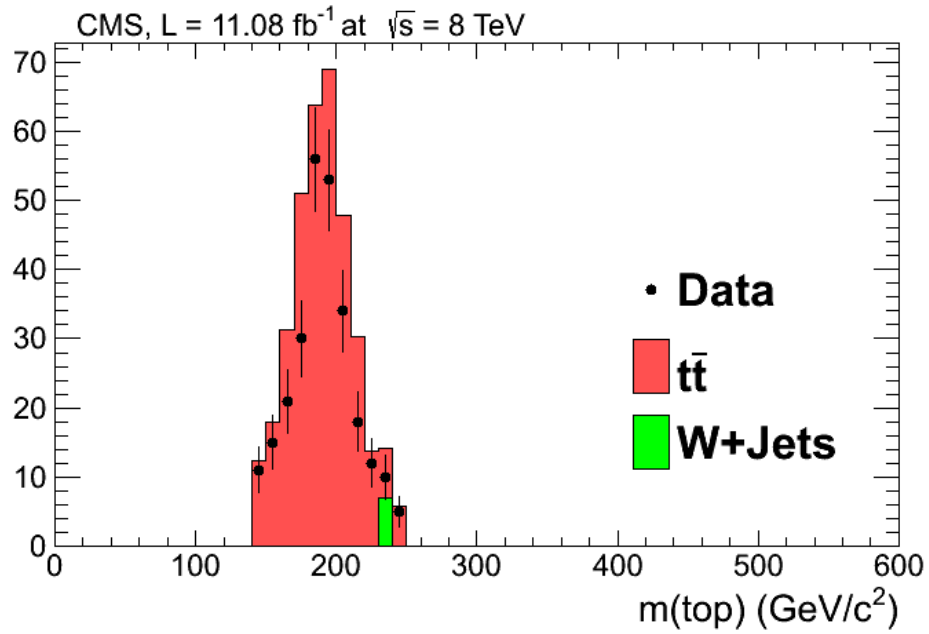


Figure 13: Mass of type 1 top candidates found in the semileptonic sample.

Sample	Dataset	Cross Section
$t\bar{t}$ + jets	/TT_Mtt-700to1000_CT10_TuneZ2star_8TeV-powheg-tauola/Summer12_DR53X-PU_S10_START53_V7A-v1/AODSIM	225 pb
$t\bar{t}$ + jets	/TT_Mtt-1000toInf_CT10_TuneZ2star_8TeV-powheg-tauola/Summer12_DR53X-PU_S10_START53_V7A-v1/AODSIM	225 pb

Table 2: Monte Carlo samples used in the analysis.

There are two  $t\bar{t}$  samples that are in use, each with a filter on the invariant mass of the  $t\bar{t}$  system. This filter efficiency is taken into account when normalizing to the expected number of events. The  $t\bar{t}$  sample used is inclusive in the top decay products, however the lepton content of the 2011 analysis was checked and is less than 1% in the final selection. Table 2 summarizes the simulated event samples used in this analysis.

## 6.2 Data-derived Backgrounds

For the QCD multijet estimate, we use a data-derived technique. This technique is identical to that described in Ref. [10] (the only difference is in the QCD mass template used in the ‘mass-modified’ procedure, described below, updated for  $\sqrt{s} = 8$  TeV), and involves selecting a sample with low SM  $t\bar{t}$  contribution. This is done by inverting the top tagging requirements on one selected jet (anti-tag) and determining the top tagging rate for the second jet (probe). This ‘anti-tag and probe’ method yields a per-jet mistag rate that is then applied to each jet in the event to determine the estimated number of QCD multijet background events. This mistag rate is parameterized as a function of jet  $p_T$ , and is shown in Figure 14. Because there is still a small contribution from SM  $t\bar{t}$  events, even after inverting the top tagging requirements on one jet, this contribution is estimated from Monte Carlo and subtracted before computing the top mistag rate.

The mistag rate is determined by the following procedure:

1. We select trijet events in the type 1+2 topology, with the leading three jets passing the thresholds 400, 200, and 30 GeV/ $c$  respectively. No requirements are made on the jet masses for the “Type 1 Top Candidate”.
2. We require that the W candidate (sub-leading jet) satisfies the jet mass criterion of the W tag, but explicitly fails the  $\mu$  cut. That is,  $\mu < 0.4$ . The pairwise mass of this W vetoed jet with nearby jet is required to pass the top mass cut ( $140 < m_{W+b} < 250$  GeV/ $c^2$ ).
3. The “Type 1” top candidate is then used as a “probe jet”.
4. The top tagging rate of the probe jet is taken as the mistag rate for the algorithm. Because W tag is explicitly vetoed, the data sample is dominated by QCD in the right kinematic regime, and is therefore an appropriate control region from which to derive the mistag rate.
5. The small contribution from continuum  $t\bar{t}$  is removed based on the Monte Carlo expectation.

Figure 14 shows the mistag rate before and after this subtraction of the SM  $t\bar{t}$  contribution.

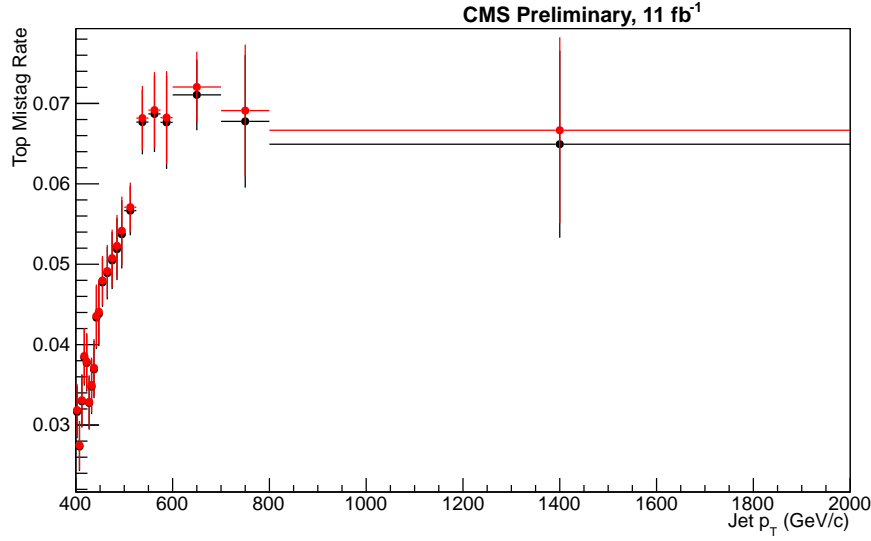


Figure 14: Mistag rate used in the determination of the QCD background, obtained with the HT750 trigger selection. The black distribution shows the rate used in the analysis, while the red distribution shows the rate determined without subtracting the residual  $t\bar{t}$  contribution.

We also show jet  $p_T$  distributions for the ensemble of jets used to determine the mistag rate. The probe and tagged jet  $p_T$  distributions are shown in Figure 15.

The single tag sample is dominated by QCD events in which probe jets originate from light quarks or gluons and typically have a low jet mass. However, the events in the signal region are required to have jet masses consistent with top quark mass, in a window between 140 and 250  $\text{GeV}/c^2$ . As  $m_{t\bar{t}}$  computed from two jets depends on their masses, if one were to use the original low mass of the probe jet in the background estimate, the shape of the estimated  $m_{t\bar{t}}$  distribution would not be correct.

In order to mimic the event kinematics of the signal region, the jet mass of the probe jet is ignored, and instead the jet mass is set to a random number drawn from a distribution of jet masses from 140 to 250  $\text{GeV}/c^2$  taken from a QCD Monte Carlo sample. This new “mass-modified-mistag” is used in the construction of the invariant mass distribution of the candidate  $t\bar{t}$  pair. This ensures that the mass of the probe jet is at least roughly similar to the mass of the equivalent jet from the signal region. Figure 16 shows this mass distribution for the 8 TeV analysis. We use the curve shown in red, which are determined using the tag and probe selection described above. This mass distribution is most kinematically similar to the sample used to estimate the QCD background.

### 6.3 Closure test of Mass-Modified procedure

In order to check that the mass-modified procedure used to estimate the QCD background is robust, we perform a closure test using a QCD Monte Carlo sample. We randomly choose a subset of roughly half the sample, from which we derive the mistag rate using the procedure derived above. With this mistag rate, we estimate the QCD background using the orthogonal subset of the QCD Monte Carlo, using the mass-modified procedure. To check the closure of this method, the QCD estimate is compared with the actual output of the QCD Monte Carlo type 1+1 selection. If this procedure is working correctly, these two distributions should be compatible within uncertainties. Figure 17 shows the result of this procedure, for both the type

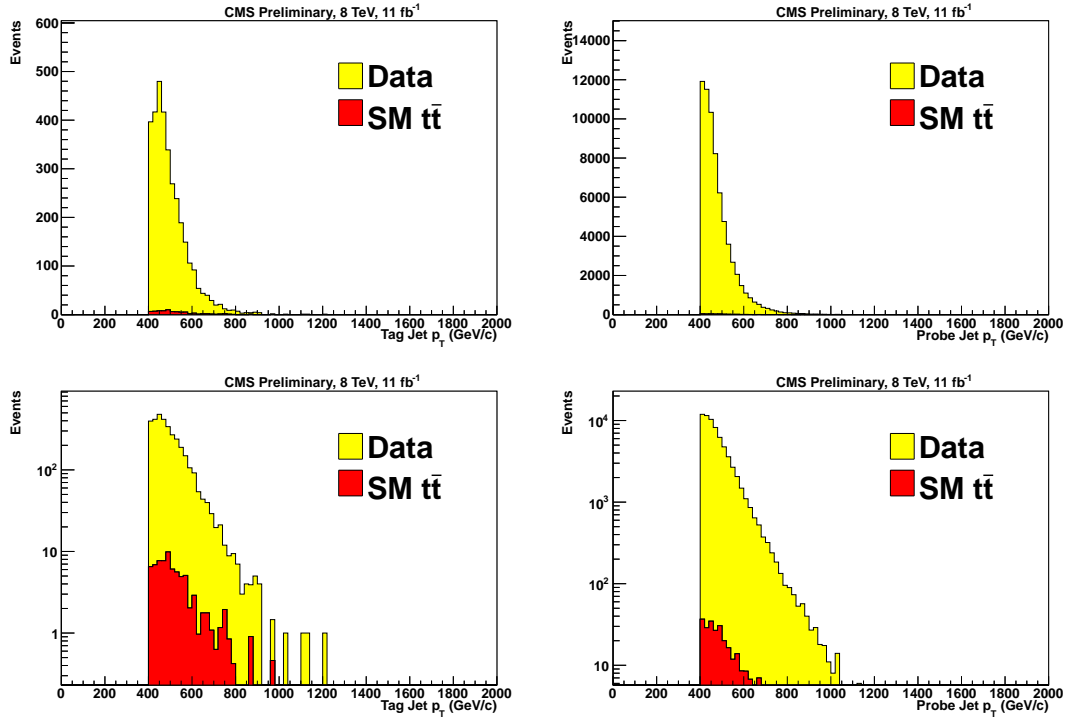


Figure 15: The numerator (tag) and denominator (probe) jet  $p_T$  distributions used to compute the mistag rate, shown in both linear(top) and logarithmic (bottom) scales.

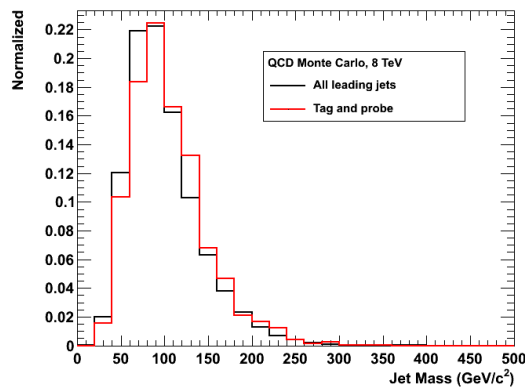


Figure 16: A comparison of the jet mass distribution, from which the jet masses are randomly assigned in the “mass-modified-mistag” procedure. The black curve is the jet mass distribution for all leading jets in the event, while the red curve shows the jet mass distributions for events passing the tag and probe selection. As the tag and probe selection is kinematically similar to that used for the QCD background estimation, we use that sample for the “mass-modified-mistag” procedure. These curves are taken from a QCD Monte Carlo sample.

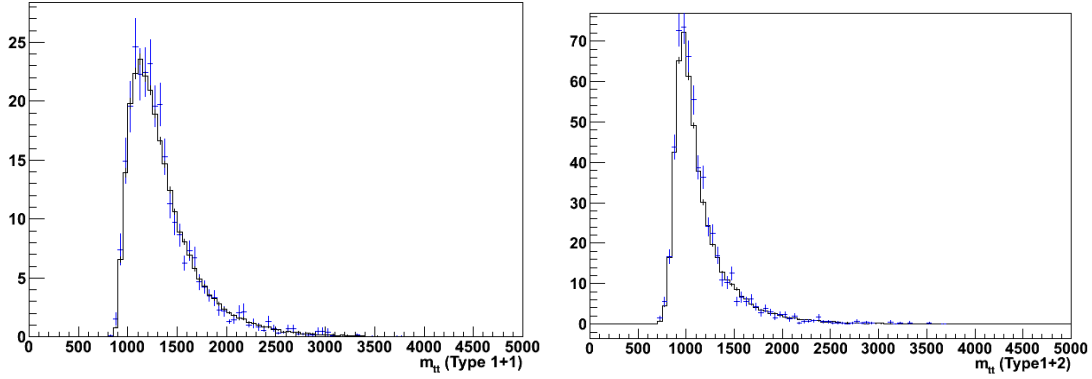


Figure 17: A closure test for the mass-modified background estimation procedure, for the type 1+1 (left) and type 1+2 (right) topologies. The histogram shows the predicted QCD  $m_{t\bar{t}}$  distribution, using the mistag procedure described in the text. The blue points show the actual QCD events passing the event selection. The two distributions are consistent within uncertainties, meaning that the mistag procedure is working correctly.

Process	Type 1+1	bfType 1+2
SM $t\bar{t}$	$347 \pm 174$	$241 \pm 121$
QCD Multijet	$4265 \pm 256$	$5136 \pm 241$
Total Background	$4612 \pm 309$	$5377 \pm 270$
Observed Data	4437	5512

Table 3: Expected numbers of background events and observed data events for the analysis. Errors include the dominant systematic uncertainties (mistag rate for QCD,  $t\bar{t}$  normalization).

1+1 and type 1+2 topologies. It can be seen that the prediction and actual QCD yields are consistent, within statistical uncertainties.

## 7 Event Yields

After estimating the background from data and Monte Carlo simulation, we proceed to form data-background comparisons for the signal and control regions – the ‘type 1+1’ and ‘type 1+2’ events, respectively. Table 3 shows the number of expected background events and observed data events for each category. Figure 18 shows some kinematic distributions for the Type 1+1 channel, while Figure 19 shows additional distributions for the type 1+2 control regions. Figure 20 shows the top pair invariant mass distribution,  $m_{t\bar{t}}$ , for type 1+1 events, while Figure 21 shows the same for the type 1+2 events. These  $m_{t\bar{t}}$  distributions are the discriminating distributions that will be used to test for the presence of a signal. In the type 1+2 distributions, the cut on the rapidity difference between the two jets has been applied, but the cleanup cuts to remove events with the anomalous tracking problem have not been applied.

## 8 Signal Samples

In this analysis, we intend to test for the presence of new physics using several models, including resonant and non-resonant production. We use both a model of RS KK gluon production [26], as well as both narrow and wide  $Z'$  resonance samples. These RS KK Gluons and  $Z'$  bosons subsequently decay to a pair of top quarks. These samples are generated using Pythia8,

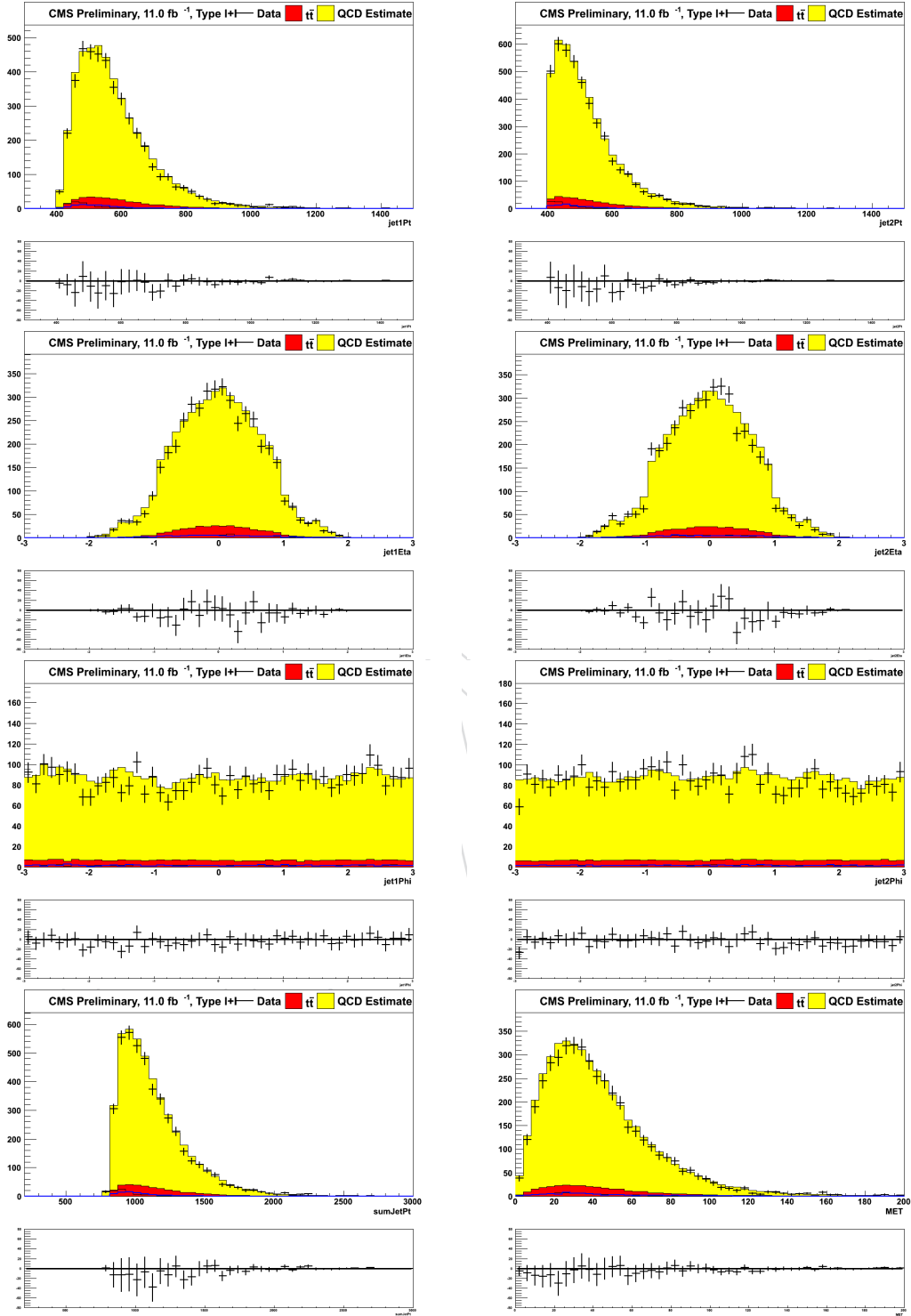


Figure 18: Kinematic distributions of the jets in the type 1+1 signal region.

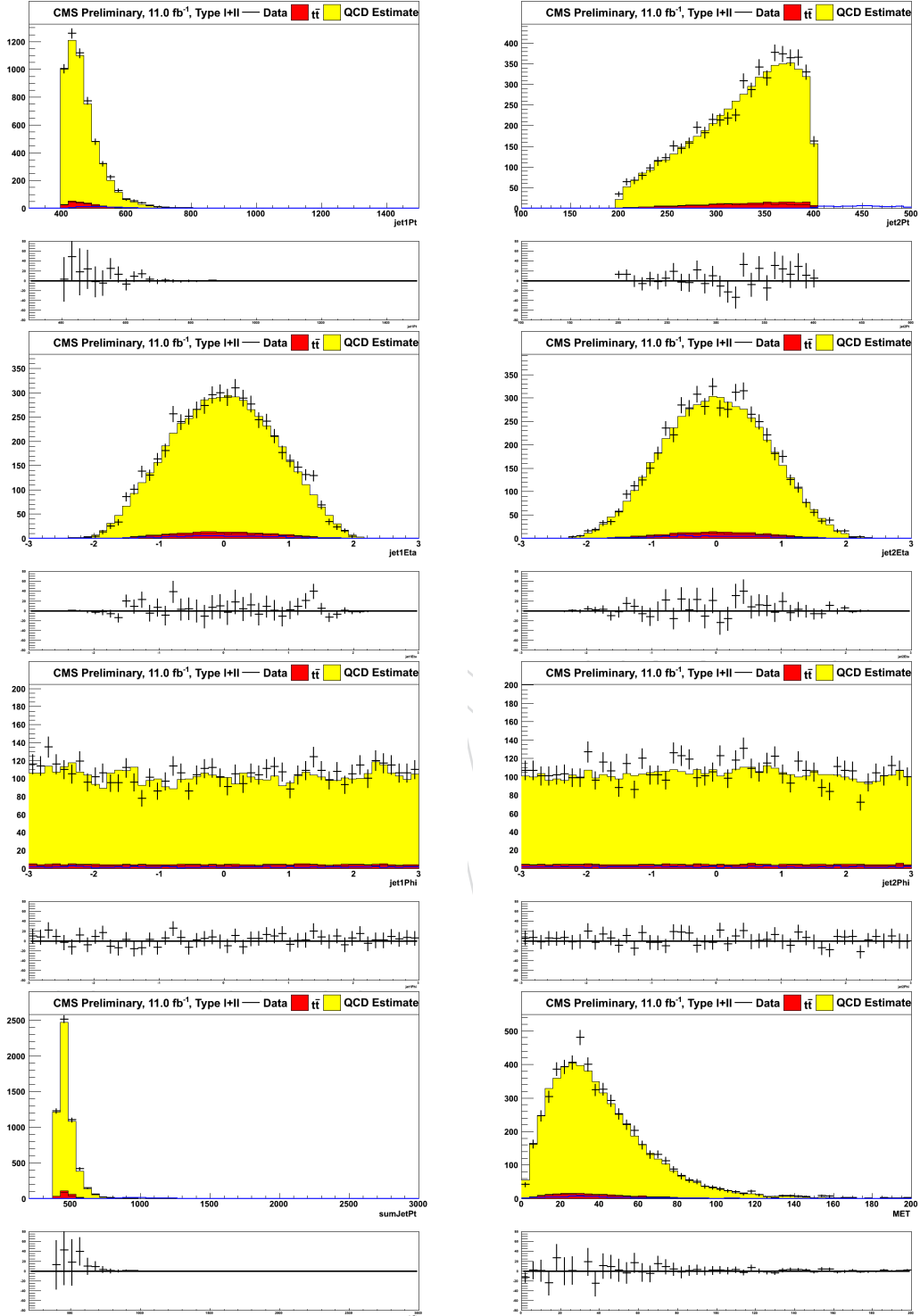


Figure 19: Kinematic distributions of the jets in the type 1+2 control region. Here, the cleanup cuts to remove events with anomalous tracking failures have not been applied.



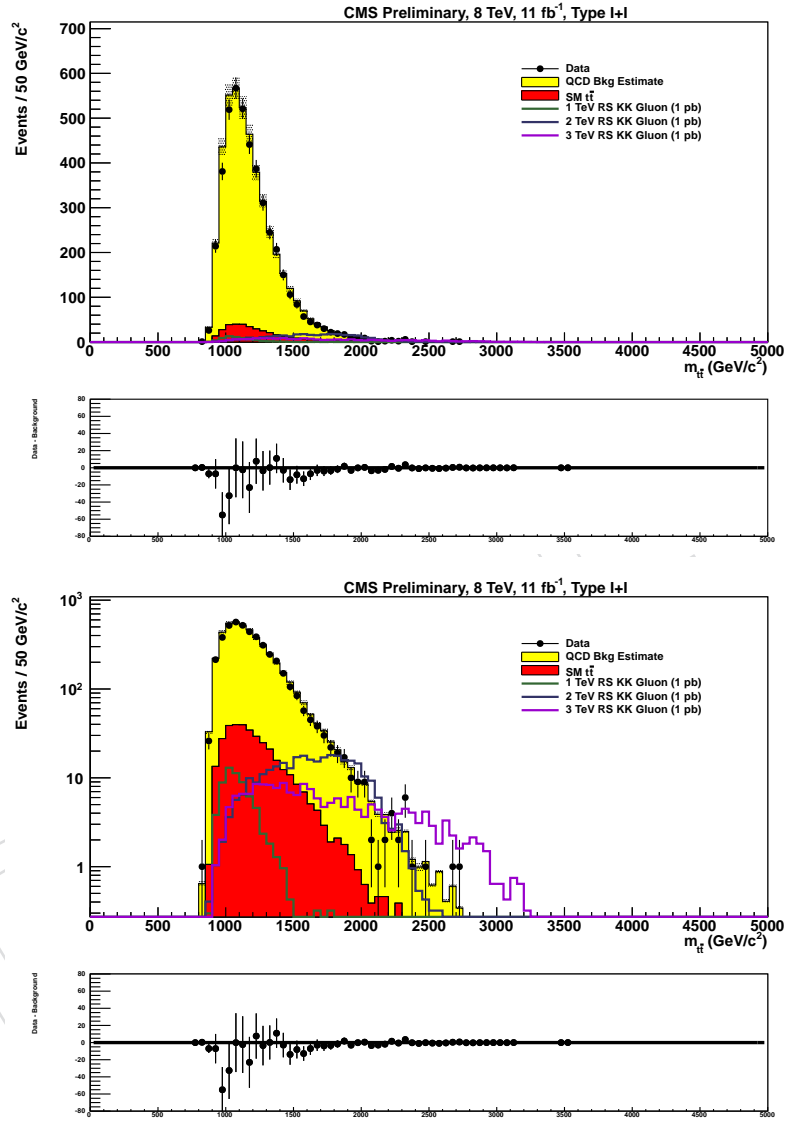


Figure 20: Distribution of the invariant mass of the reconstructed top quark pair,  $m_{t\bar{t}}$ , for Type 1+1 candidate events, shown in linear (top) and log (bottom) scales. The lower plot in each case shows the ratio of the observed data to expected background in each bin of the histogram. The gray shaded region represents the systematic uncertainty on the background model.

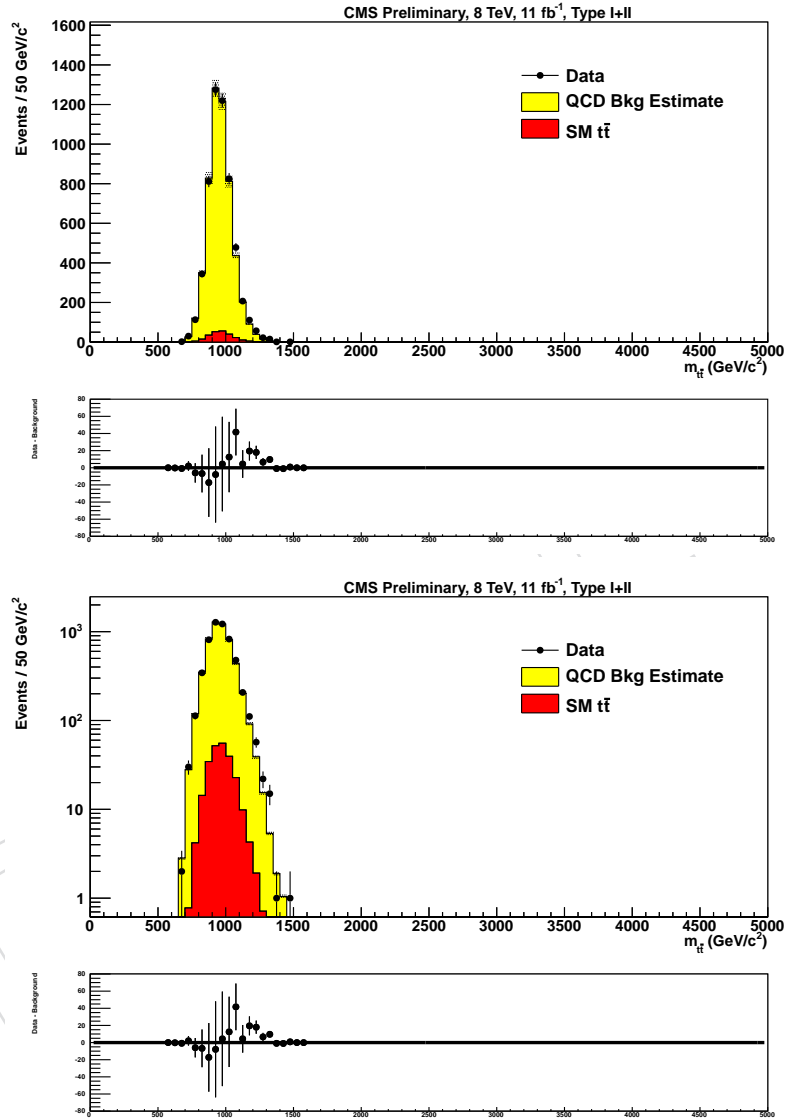


Figure 21: Distribution of the invariant mass of the reconstructed top quark pair,  $m_{t\bar{t}}$ , for Type 1+2 candidate events, shown in linear (top) and log (bottom) scales. The lower plot in each case shows the ratio of the observed data to expected background in each bin of the histogram. The gray shaded region represents the systematic uncertainty on the background model.

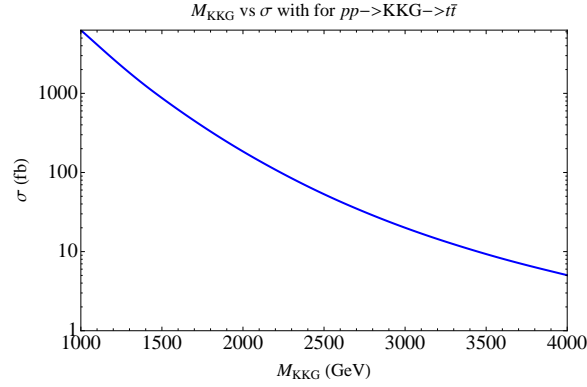


Figure 22: RS KK Gluon cross sections for a center of mass energy of 8 TeV. Computation done as in [26], updated to 8 TeV upon private communication with authors.

for masses of 1, 1.5, 2, 3, and 4 TeV/ $c^2$ . Table 4 summarizes the signal samples used in this analysis. The listed cross sections for the RS Gluon are obtained from the authors of Ref. [26], updated for a center of mass energy of 8 TeV in a private communication. Figure 22 shows a plot of the RS KK Gluon cross sections as a function of the KK Gluon mass.

Figures 23-25 shows kinematic distributions of the signal samples, to display the behavior across the different mass points in this analysis. We show several of the jet substructure quantities for the RS KK Gluon samples.

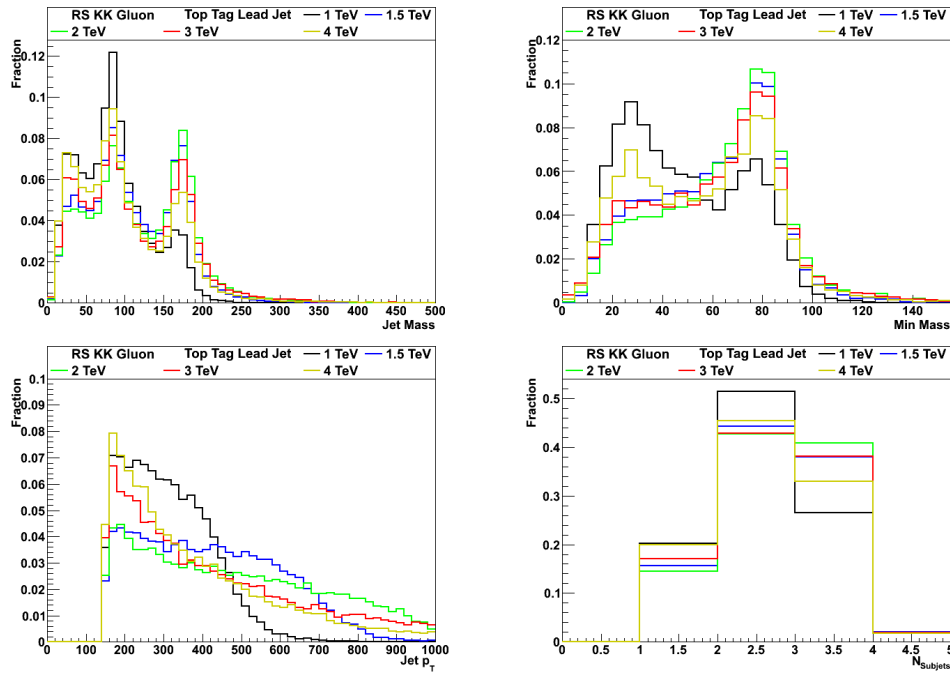


Figure 23: Kinematic distributions for the RS KK Gluon samples, for the leading jet considered in the top tagging algorithm.

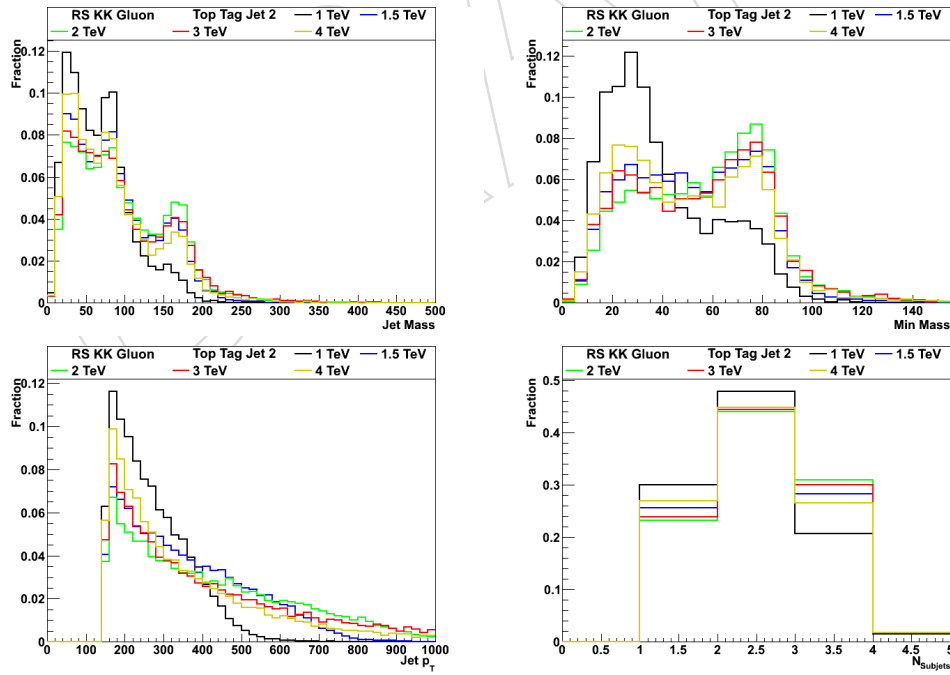


Figure 24: Kinematic distributions for the RS KK Gluon samples, for the sub-leading jet considered in the top tagging algorithm.

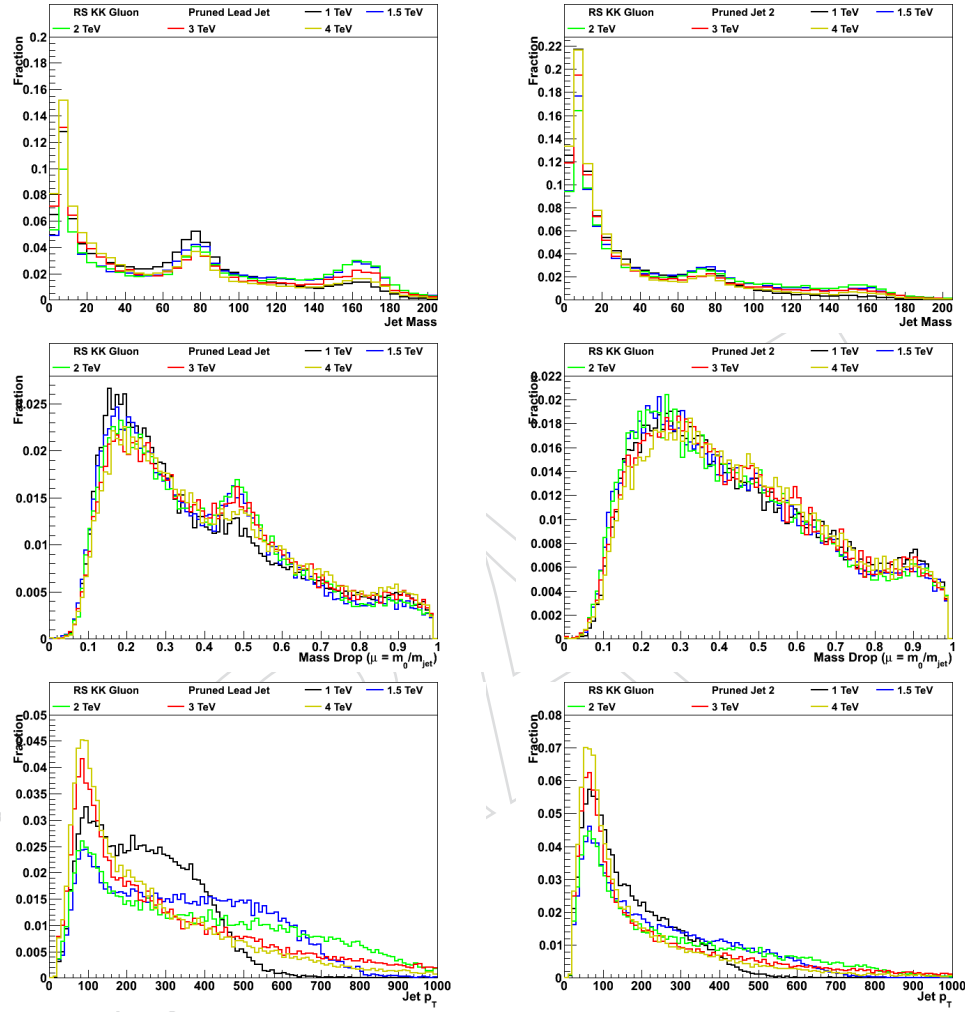


Figure 25: Kinematic distributions for the RS KK Gluon samples, for the leading and sub-leading jets considered with the jet pruning algorithm.

Sample	Dataset	Mass	Cross Section
RS KK Gluon	/Pythia8_RSGluonToTTbar_M_1000_8TeV	1 TeV/ $c^2$	6.299 pb
RS KK Gluon	/Pythia8_RSGluonToTTbar_M_1500_8TeV	1.5 TeV/ $c^2$	0.828 pb
RS KK Gluon	/Pythia8_RSGluonToTTbar_M_2000_8TeV	2 TeV/ $c^2$	0.182 pb
RS KK Gluon	/Pythia8_RSGluonToTTbar_M_3000_8TeV	3 TeV/ $c^2$	0.021 pb
RS KK Gluon	/Pythia8_RSGluonToTTbar_M_4000_8TeV	4 TeV/ $c^2$	0.005 pb
Narrow $Z'$	/ZPrimeToTTJets_M1000GeV_W10GeV	1 TeV/ $c^2$	–
Narrow $Z'$	/ZPrimeToTTJets_M1500GeV_W15GeV	1.5 TeV/ $c^2$	–
Narrow $Z'$	/ZPrimeToTTJets_M2000GeV_W20GeV	2 TeV/ $c^2$	–
Narrow $Z'$	/ZPrimeToTTJets_M3000GeV_W30GeV	3 TeV/ $c^2$	–
Narrow $Z'$	/ZPrimeToTTJets_M4000GeV_W40GeV	4 TeV/ $c^2$	–
Wide $Z'$	/ZPrimeToTTJets_M1000GeV_W100GeV	1 TeV/ $c^2$	–
Wide $Z'$	/ZPrimeToTTJets_M1500GeV_W150GeV	1.5 TeV/ $c^2$	–
Wide $Z'$	/ZPrimeToTTJets_M2000GeV_W200GeV	2 TeV/ $c^2$	–
Wide $Z'$	/ZPrimeToTTJets_M3000GeV_W300GeV	3 TeV/ $c^2$	–
Wide $Z'$	/ZPrimeToTTJets_M4000GeV_W400GeV	4 TeV/ $c^2$	–

Table 4: Signal samples used in the analysis.

We also study the selection efficiency of the signal samples used in the analysis. Table 5 shows the signal efficiencies for the RS Gluon samples used in the analysis, after each successive cut is applied in the event selection.

We apply the same selection described above to the signal samples, to obtain distributions of  $m_{\tilde{t}\tilde{t}}$  for the type 1+1 and type 1+2 signal events. Figure 26 shows the  $m_{\tilde{t}\tilde{t}}$  distribution for selected RS KK gluon events in the type 1+1 topology. Figure 28 shows the  $m_{\tilde{t}\tilde{t}}$  distribution for the narrow  $Z'$  signal samples, in the type 1+1 topology.

In the type 1+1 case for RS Gluons, it can be seen that for high mass points, the distribution does not peak at the RS KK gluon mass. This is due to the off-shell component in the RS KK gluon production, which enters into the tails of the distribution and appears at low mass values. For the type 1+2 events, this effect is also present, but for high mass points, the type 1+2 events start to migrate to the type 1+1 channel, as the jets begin to merge even closer together. This is why the distributions all peak at 1-1.5 TeV, in the type 1+2 channel.

TYPE 1+1 – RS GLUON

Sample	Jet $p_T > 400$	$ \eta  < 2.4,  \Delta y  < 1.0$	$\Delta\phi > 2.1$	$140 < m_{\text{jet}} < 250$	$N_{\text{sub}} > 2$	$m_{\text{min}} > 50$
TTJets	0.12%	0.07%	0.07%	0.03%	0.02%	0.01%
RSG (1 TeV)	6.51%	4.89%	4.87%	1.44%	0.98%	0.73%
RSG (1.5 TeV)	23.76%	14.53%	14.48%	5.67%	3.67%	2.97%
RSG (2 TeV)	28.96%	16.05%	15.94%	6.51%	3.91%	3.11%
RSG (2.5 TeV)	26.84%	14.47%	14.36%	5.62%	3.24%	2.46%
RSG (3 TeV)	21.89%	11.82%	11.70%	4.40%	2.55%	1.85%
RSG (3.5 TeV)	17.33%	9.53%	9.45%	3.57%	2.15%	1.56%
RSG (4 TeV)	14.63%	8.35%	8.28%	2.99%	1.83%	1.41%

TYPE 1+1 – NARROW  $Z'$ 

Sample	Jet $p_T > 400$	$ \eta  < 2.4,  \Delta y  < 1.0$	$\Delta\phi > 2.1$	$140 < m_{\text{jet}} < 250$	$N_{\text{sub}} > 2$	$m_{\text{min}} > 50$
TTJets	0.12%	0.07%	0.07%	0.03%	0.02%	0.01%
$Z'$ (1 TeV)	8.40%	6.89%	6.87%	2.24%	1.30%	0.95%
$Z'$ (1.5 TeV)	38.45%	22.85%	22.75%	10.26%	6.19%	5.10%
$Z'$ (2 TeV)	55.70%	29.08%	28.80%	12.42%	6.75%	5.44%
$Z'$ (3 TeV)	66.46%	31.73%	31.20%	10.72%	5.94%	3.33%
$Z'$ (4 TeV)	38.99%	19.09%	18.83%	5.96%	3.70%	1.98%

TYPE 1+1 – WIDE  $Z'$ 

Sample	Jet $p_T > 400$	$ \eta  < 2.4, -\Delta y  < 1.0$	$\Delta\phi > 2.1$	$140 < m_{\text{jet}} < 250$	$N_{\text{sub}} > 2$	$m_{\text{min}} > 50$
TTJets	0.12%	0.07%	0.07%	0.03%	0.02%	0.01%
$Z'$ (1 TeV)	7.83%	6.18%	6.16%	2.08%	1.24%	0.93%
$Z'$ (1.5 TeV)	31.80%	19.18%	19.08%	8.39%	5.17%	4.21%
$Z'$ (2 TeV)	42.80%	23.15%	22.97%	10.01%	5.56%	4.45%
$Z'$ (3 TeV)	36.99%	19.14%	18.91%	7.16%	3.95%	2.74%
$Z'$ (4 TeV)	22.80%	12.67%	12.55%	4.81%	2.81%	2.03%

Table 5: Signal efficiencies for type 1+1 events, both for RS Gluon samples (top), narrow  $Z'$  samples (center), and wide  $Z'$  samples (bottom).



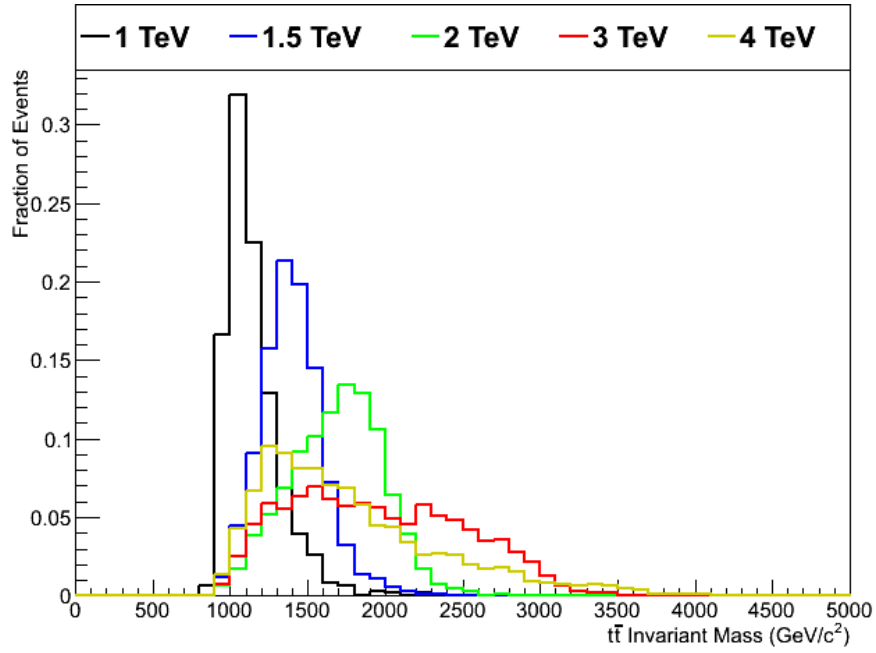


Figure 26: Distribution of the invariant mass of the reconstructed top quark pair in RS KK Gluon simulated events,  $m_{t\bar{t}}$ , for Type 1+1 candidate events.

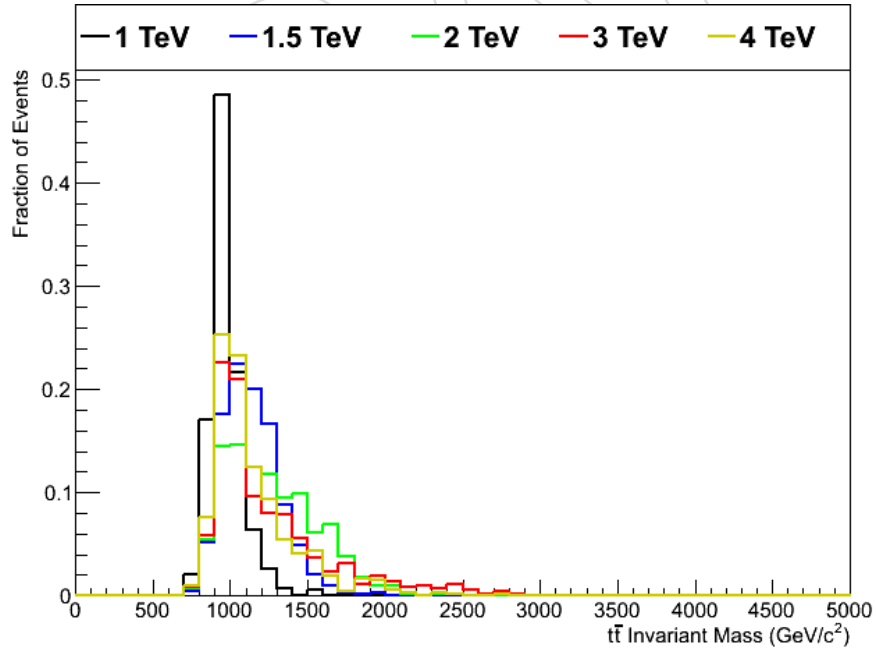


Figure 27: Distribution of the invariant mass of the reconstructed top quark pair in RS KK Gluon simulated events,  $m_{t\bar{t}}$ , for Type 1+2 candidate events.

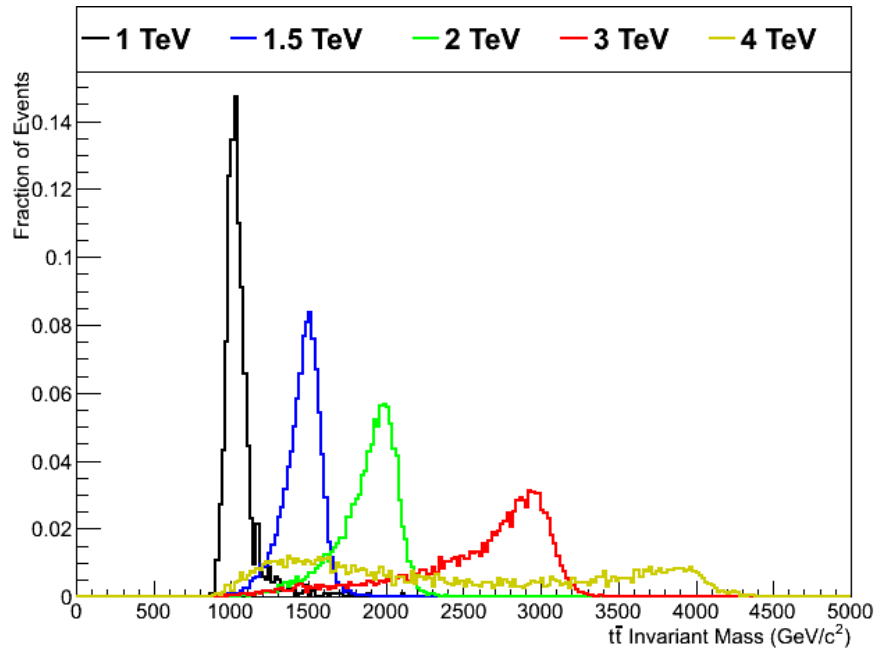


Figure 28: Distribution of the invariant mass of the reconstructed top quark pair in  $Z'$  simulated events,  $m_{t\bar{t}}$ , for Type 1+2 candidate events.

## 9 Systematic Uncertainties

We evaluate several sources of systematic uncertainty, both on the signal samples used in the analysis, and on the methods used to estimate the background composition. This section will detail the systematic uncertainties applied in this analysis. We account for rate systematics, affecting the overall normalization of signal or background processes, as well as shape systematic uncertainties, which affect the reconstructed  $t\bar{t}$  invariant mass, as well as the overall normalization. Table 6 summarizes the various systematic uncertainties applied to the samples used in the analysis, and the effect due to each.

### 9.1 Trigger Efficiency

The trigger efficiency applied to simulated events is measured by simulating the trigger behavior on simulated events. The resulting trigger efficiency curve is shown in Figure 2. Because the trigger is nearly fully efficient in the type 1+1 selection, we do not use a shape-based approach for this systematic. Instead, we apply a flat uncertainty of 2% to cover the trigger efficiency. This systematic uncertainty has a small effect for the type 1+1 channel – this is because the jet  $p_T$  cuts select events mainly above the turn-on region of the trigger efficiency curve.

### 9.2 Jet Energy Scale

We evaluate the effect of the jet energy scale uncertainty on the simulated samples. This is done by varying the jet four-momentum up and down by the jet energy scale uncertainty, which is approximately 5%. We include  $p_T$  and  $\eta$  dependent corrections to the jet energies, combined with uncertainties due to the difference in the  $W$  mass for data and Monte Carlo, along with uncertainties on the response of the pruning algorithm for jets in data and simulation. This combination of uncertainties is described in [10]. This results in a shape difference in the  $m_{t\bar{t}}$  spectrum, which depends on the invariant mass itself. For low masses, the effect is large since the jets are close to the  $p_T$  cut of 400 GeV/ $c$ . Varying the four-momenta causes jets to fall below the cut, or be promoted above the cut – increasing or decreasing acceptance. For higher invariant masses, the jets generally have higher  $p_T$  and this effect is smaller. This systematic uncertainty is applied to both the signal samples and the SM  $t\bar{t}$  sample.

Figure 29 shows the jet energy scale systematic shapes for the signal sample, while Figure 30 shows the same for the SM  $t\bar{t}$  sample.

### 9.3 Jet Energy Resolution

We account for differing jet energy resolutions between simulated events and data events. A default smearing of the jet  $p_T$  values by 10% is applied to simulated events. The uncertainty on this smearing value is roughly 10%, so we form systematic shape uncertainties by applying smearings of 0% and 20%. This systematic uncertainty is applied only to the signal samples, and the systematic shapes can be seen in Figure 31. Additionally, we assume that the jet energy resolution for subjets is the same as that for the hard jets. The variation of the subjet  $p_T$  is also included in these shape uncertainties. The effect of this systematic is not significant, and is neglected in the final limit calculation.

### 9.4 Jet Angular Resolution

Similar to the jet energy resolution, we also study the effect of the differing angular resolution between data and simulation. A smearing of the jet  $\eta$  values is done, with the central value being 10%, and systematic shapes formed by changing this value to 0% or 20%. As with the jet

TYPE 1+1 EVENTS

Systematic Source	Process Mass (TeV/ $c^2$ )	$t\bar{t}$	QCD	RS KK Gluon							
	Variation			1	1.5	2	2.5	3	3.5	4	
Effect of Systematic											
Trigger Efficiency	2	2		2	2	2	2	2	2	2	2
Jet Energy Scale	$\sim \pm 5$	$+11$ $-15$		$+15$ $-21$ $+0.2$ $+0.8$ $5$	$+1.4$ $-2.7$ $-0.6$ $+0.2$ $5$	$-4.9$ $+0.2$ $-0.7$ $+0.9$ $5$	$-5.7$ $+0.8$ $-0.4$ $+1.0$ $5$	$-3.4$ $-0.1$ $-0.7$ $+0.4$ $5$	$-2.6$ $-3.7$ $-0.9$ $+0.3$ $5$	$-3.3$ $-4.0$ $+0.0$ $+0.8$ $5$	2
Jet Energy Resolution	$10 \pm 10$										
Luminosity	$\pm 5$	5									
Subjet Scale Factor	$99 \pm 5$	5		5	5	5	5	5	5	5	5
QCD Determination	See Text		4.7								
$t\bar{t}$ Cross Section	$\pm 50$	50									

	Process	Z' (1% Width)				Z' (10% Width)					
	Variation	1	1.5	2	3	4	1	1.5	2	3	4
Systematic Source	Variation	Effect of Systematic									
Trigger Efficiency	2	2	2	2	2	2	2	2	2	2	2
Jet Energy Scale	$\sim \pm 5$	+21 -24 +0.4 -0.2 5	-2.1 -1.4 -0.1 +0.5 5	-8.3 +3.1 -0.3 +0.5 5	-15 +9.1 -1.1 +1.0 5	-10 +2.6 -0.6 +0.6 5	+17 -22 +0.1 +0.4 5	-1.3 +3.2 -0.4 +0.3 5	-6.1 +2.7 -0.6 +0.6 5	-7.8 +4.6 -0.7 +0.6 5	2 -3.9 +0.7 -0.6 +0.8 5
Jet Energy Resolution	$10 \pm 10$										
Luminosity	$\pm 5$	5	5	5	5	5	5	5	5	5	5
Subjet Scale Factor	$99 \pm 5$	5	5	5	5	5	5	5	5	5	5
QCD Determination	See Text										
$t\bar{t}$ Cross Section	$\pm 50$										

Table 6: Systematic uncertainties applied to the analysis. All values are in percent and symmetric unless otherwise indicated.

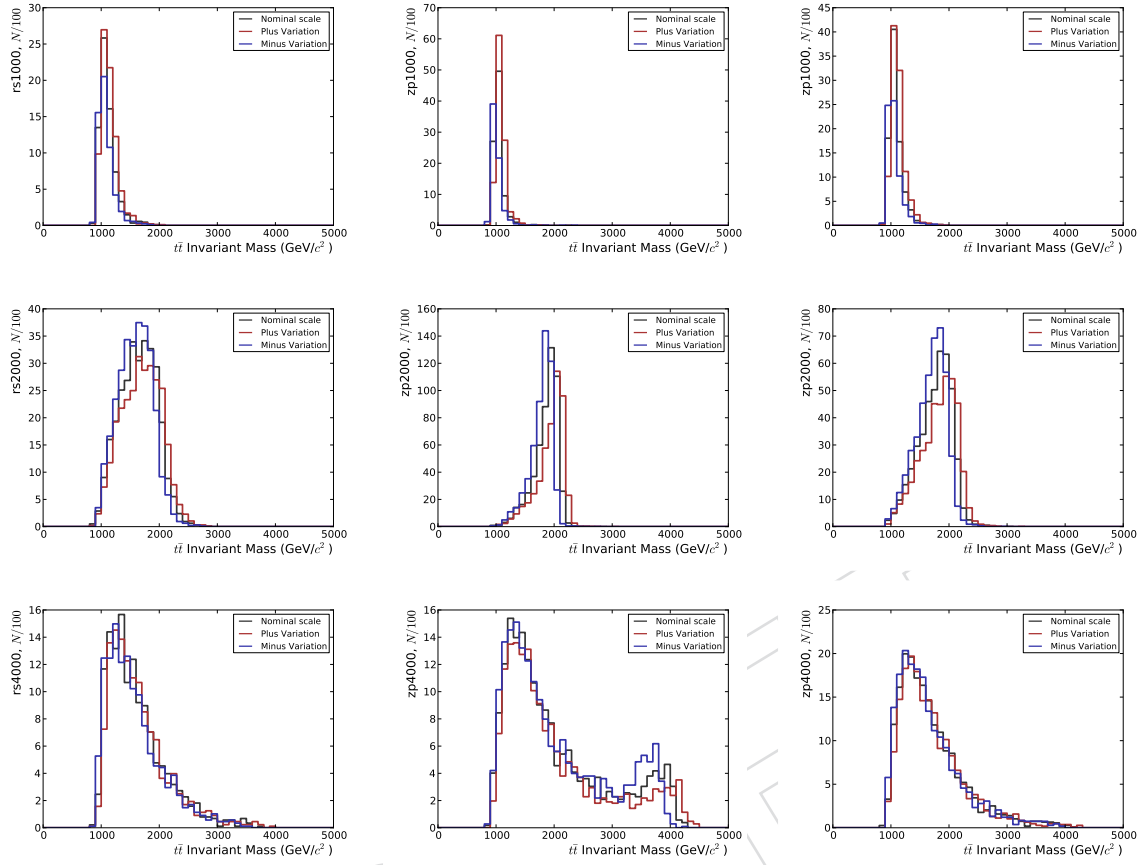


Figure 29: Systematic shape uncertainties on the jet energy scale for the signal samples. RS Gluon events are shown in the left column, narrow  $Z'$  events are shown in the center column, and wide  $Z'$  events in the right column.

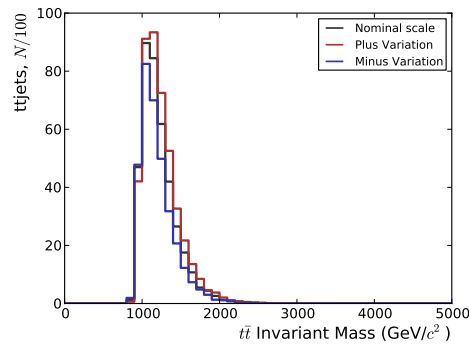


Figure 30: Systematic shape uncertainty on the jet energy scale for the  $t\bar{t}$  sample.

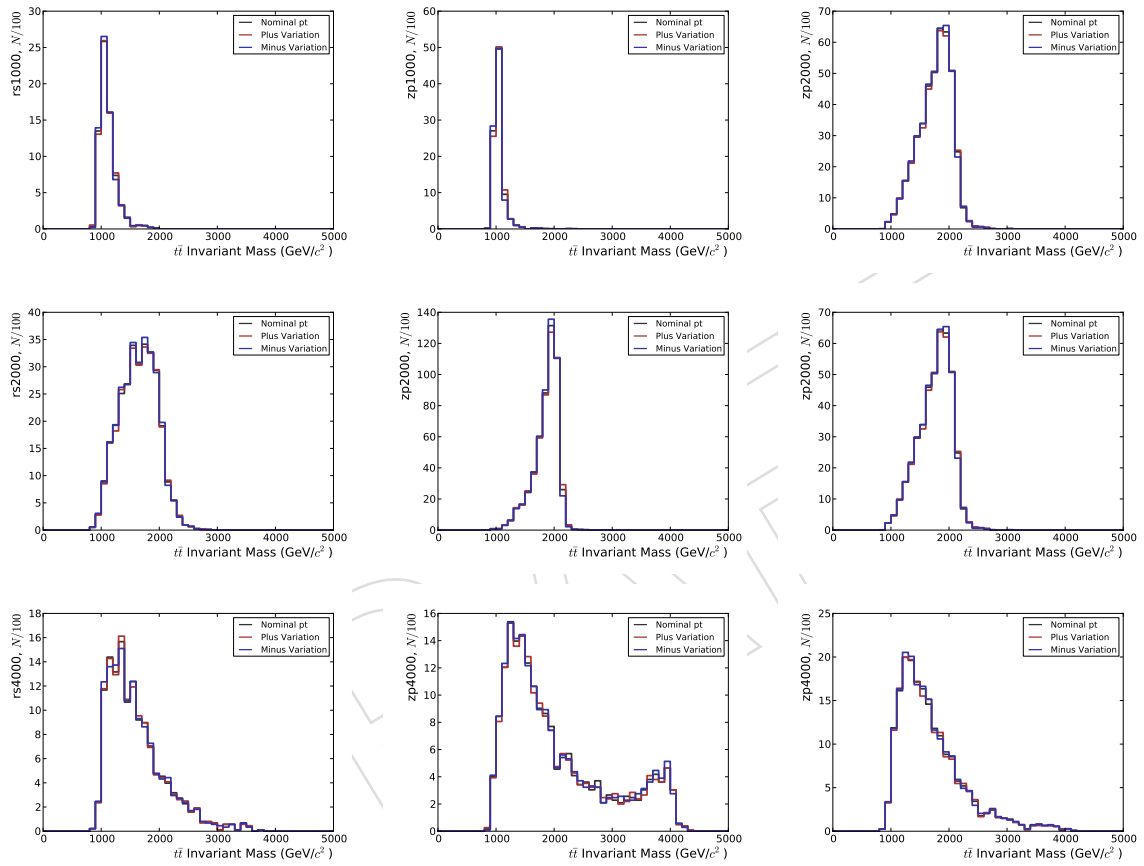


Figure 31: Systematic shape uncertainties on the jet energy resolution for some type 1+1 signal samples ( $m = 1, 2, 4 \text{ TeV}/c^2$ ). The left column shows RS Gluon samples, the center column shows the narrow  $Z'$  sample, and the right column shows the wide  $Z'$  sample, for the same mass value.

energy resolution, this effect is taken to be the same for the hard jets and the subjets. The effect is not significant and the systematic uncertainty is neglected in the final limit calculation.

### 9.5 Substructure Selection Efficiency

As described above, we measure a scale factor for the subjet jet energy scale and selection efficiency, using a semileptonic sample. Working under the assumption that these values are identical for both the top tagging and W tagging algorithms, we therefore need to double the effect of the selection efficiency scale factor determined above. This uncertainty is a rate-only uncertainty and is applied to both the signal samples as well as the SM  $t\bar{t}$  sample.

### 9.6 SM $t\bar{t}$ Normalization Uncertainty

The effect of the renormalization and factorization scales ( $Q^2$ ) was studied in the previous version of this analysis [10]. Variations of approximately 50% were observed when varying up and down these  $Q^2$  values. A normalization difference was observed in these samples, but the shape of the  $m_{t\bar{t}}$  distribution was not affected by the variation of the renormalization and factorization scales. In addition, comparisons of theoretical predictions of the  $t\bar{t}$  cross section in this high- $p_T$  regime give discrepancies of approximately 50% as well. We keep the same uncertainty of 50% on the normalization of the SM  $t\bar{t}$  sample used in this analysis.

### 9.7 QCD Estimation Uncertainty

As described above, we use a data-based method to estimate the QCD contribution to the final signal selections in the analysis. This is done using a procedure where the substructure tagging requirements are inverted ('anti-tag and probe' method), however the jet mass is set by hand to be in the range [140, 250] GeV/ $c^2$ . The mass is drawn randomly from a template constructed from a QCD Monte Carlo sample.

To account for systematic uncertainties when using this method, we determine the change when switching to an alternate method. The alternate method follows the same procedure, without setting the jet mass by hand. The jet mass is kept as its original value after inverting the substructure tagging requirements. The systematic uncertainty is then taken as half the difference between these two methods. Figure 32 shows the differences obtained when using these two methods. The effect on the normalization is approximately 3.5% for type 1+1 events, and is larger at approximately 10% for type 1+2 events. In addition to this systematic uncertainty, we also include the statistical uncertainty from the observed number of data events used in the determination of the QCD mistag contribution.

## 10 Statistical Interpretation and Results

As we do not observe any excess of data above the expected background contribution, we proceed to set limits on the production cross sections of the RS KK Gluon and  $Z'$  models used in this analysis. We compare the number of observed events,  $N_{obs}$ , to the expected number of signal events,  $N_{exp}$ , where the quantity  $N_{exp}$  is determined according to the following formula:

$$N_{exp} = \sigma_{RS} \cdot \mathcal{B}(t\bar{t}) \cdot \epsilon \cdot L$$

Here,  $\sigma_{RS}$  represents the expected production cross section of the RS KK Gluon model,  $\mathcal{B}$  is the branching fraction to top quark pairs,  $\epsilon$  is the signal selection efficiency, and  $L$  is the integrated luminosity of the dataset being analyzed.



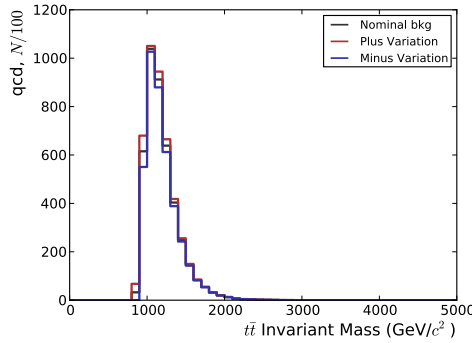


Figure 32: Systematic shape uncertainty on the QCD background estimate, obtained by using two different data-based methods in the type 1+1 channel.

We perform a shape analysis using the  $m_{t\bar{t}}$  invariant mass distribution. This shape analysis compares the signal model distribution with the Standard Model expectation (QCD and continuum  $t\bar{t}$  production), allowing the various components to fluctuate within their systematic and statistical uncertainties.

We use the theta framework [27] to produce 95% CL upper limits on the RS KK Gluon cross section, using a Bayesian method. A Poisson model is used for each bin in the  $m_{t\bar{t}}$  distribution. The likelihood function is composed of the product of the Poisson probabilities for all the bins in the  $m_{t\bar{t}}$  distribution. For a single bin, the mean of the Poisson distribution is given as

$$\mu_i = \sum_k \beta_k \cdot T_{k,i},$$

where the sum over  $k$  includes all the components of the background model,  $T$  represents the number of expected events for process  $k$  in bin  $i$ , normalized by the expected cross section and integrated luminosity. The factor  $\beta$  is the Poisson mean for the individual process  $k$ . Therefore, to form the full likelihood function, one must multiply these factors over all the bins in the  $m_{t\bar{t}}$  distributions:

$$\mathcal{L}(\beta_k) = \prod_i^{N_{bins}} \frac{\mu_i \cdot e^{-\mu_i}}{N_i^{data}!}$$

For the individual Poisson parameters  $\beta_k$ , we use different choices of prior distributions. For the QCD estimate, as well as the signal cross section, a flat prior is used. For the Standard model  $t\bar{t}$  contribution, a lognormal prior distribution is used, with a 15% width, matching the uncertainty on the  $t\bar{t}$  cross section.

Using these parameters, we perform pseudoexperiments to estimate the 68% and 95% CL (1- and 2- $\sigma$ ) expected limit bands. In the pseudoexperiments, the systematic effects are accounted for through nuisance parameters. These nuisance parameters are randomly varied within their uncertainties, and the posterior is refitted for each pseudoexperiment. This process allows for the evaluation of the effect of both shape and normalization uncertainties.

Figure 33 shows the expected and observed results, along with the 1- and 2- $\sigma$  expected limit bands, obtained using the method described here, for the RS Gluon hypothesis. These results are also summarized in Table 7. Figure 34 and Table 8 show the results for the narrow  $Z'$  hypothesis. Figure 35 and Table 9 show the results for the wide  $Z'$  hypothesis.

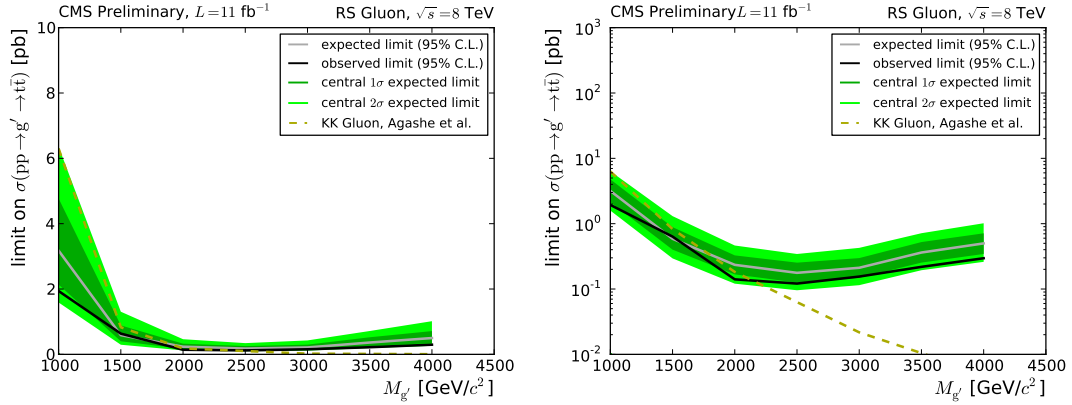


Figure 33: Preliminary expected and observed limits, in linear (left) and logarithmic (right) scales, for the RS Gluon hypothesis. The theory expectation is shown in the dotted curve.

RS GLUON HYPOTHESIS						
Mass (TeV/ $c^2$ )	Observed Limit	Expected Limits				
		-2 $\sigma$	-1 $\sigma$	Median	+1 $\sigma$	+2 $\sigma$
1.0	<b>1.94</b>	1.59	2.13	<b>3.18</b>	4.77	6.36
1.5	<b>0.63</b>	0.29	0.40	<b>0.59</b>	0.88	1.30
2.0	<b>0.14</b>	0.12	0.17	<b>0.23</b>	0.33	0.46
2.5	<b>0.12</b>	0.096	0.13	<b>0.18</b>	0.25	0.34
3.0	<b>0.16</b>	0.11	0.15	<b>0.21</b>	0.30	0.43
3.5	<b>0.22</b>	0.19	0.25	<b>0.36</b>	0.52	0.71
4.0	<b>0.30</b>	0.26	0.34	<b>0.50</b>	0.71	1.02

Table 7: Expected and observed limits on the production cross section, in units of pb, for the RS Gluon hypothesis.

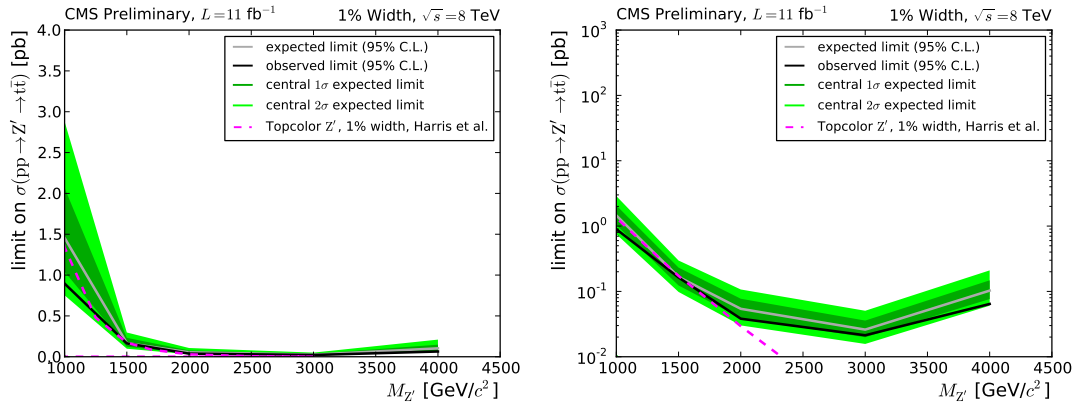


Figure 34: Preliminary expected and observed limits, in linear (left) and logarithmic (right) scales, for the narrow  $Z'$  hypothesis. The theory expectation is shown in the dotted curve.

### NARROW Z' HYPOTHESIS

Mass (TeV/ $c^2$ )	Observed Limit	Expected Limits				
		$-2\sigma$	$-1\sigma$	Median	$+1\sigma$	$+2\sigma$
1.0	<b>0.896</b>	0.752	1.041	<b>1.455</b>	2.067	2.880
1.5	<b>0.163</b>	0.098	0.123	<b>0.166</b>	0.231	0.296
2.0	<b>0.038</b>	0.030	0.039	<b>0.054</b>	0.077	0.107
3.0	<b>0.021</b>	0.015	0.020	<b>0.026</b>	0.036	0.051
4.0	<b>0.064</b>	0.060	0.076	<b>0.102</b>	0.147	0.209

Table 8: Expected and observed limits on the production cross section, in units of pb, for the RS Gluon hypothesis.

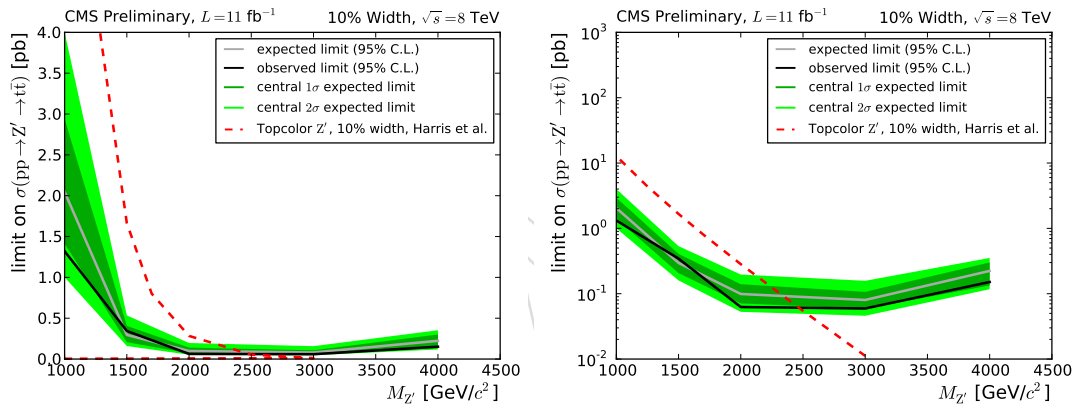


Figure 35: Preliminary expected and observed limits, in linear (left) and logarithmic (right) scales, for the narrow Z' hypothesis. The theory expectation is shown in the dotted curve.

### WIDE Z' HYPOTHESIS

Mass (TeV/ $c^2$ )	Observed Limit	Expected Limits				
		$-2\sigma$	$-1\sigma$	Median	$+1\sigma$	$+2\sigma$
1.0	<b>1.321</b>	1.002	1.415	<b>2.048</b>	2.941	4.000
1.5	<b>0.344</b>	0.159	0.207	<b>0.296</b>	0.406	0.534
2.0	<b>0.063</b>	0.053	0.071	<b>0.099</b>	0.140	0.196
3.0	<b>0.059</b>	0.046	0.059	<b>0.080</b>	0.107	0.158
4.0	<b>0.151</b>	0.117	0.133	<b>0.223</b>	0.301	0.353

Table 9: Expected and observed limits on the production cross section, in units of pb, for the wide Z' hypothesis.

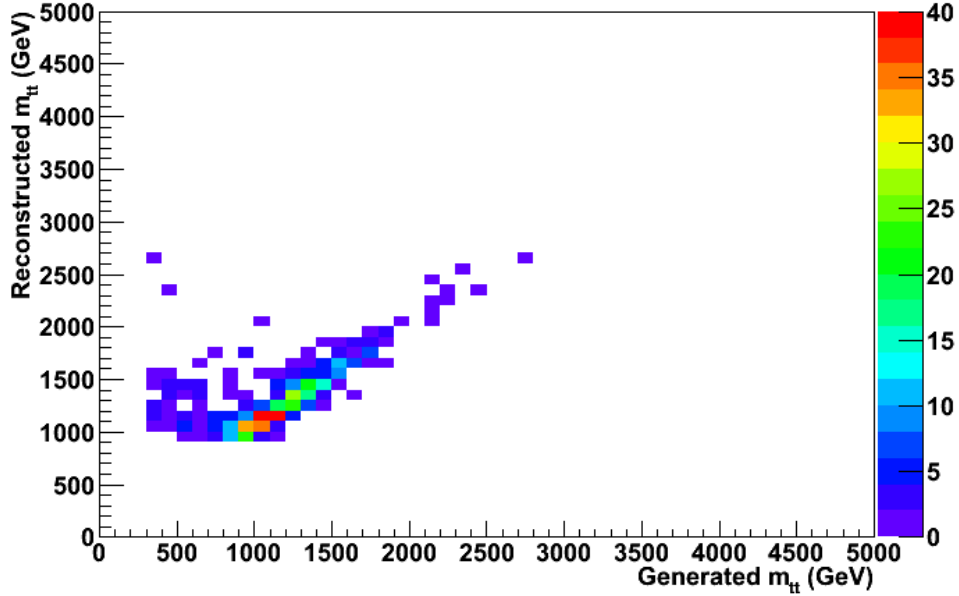


Figure 36: Reconstructed vs. generated  $m_{t\bar{t}}$  distributions, used to correct for efficiency and acceptance effects. This plot shows type 1+1 events.

### 10.1 $m_{t\bar{t}}$ Spectrum Enhancement Analysis

In addition to using the  $m_{t\bar{t}}$  spectrum to set limits on the presence of new physics models in the form of resonances, we also conduct another analysis involving the presence of a new physics model which causes a general non-resonant enhancement of the  $m_{t\bar{t}}$  spectrum. As this enhancement is predicted to arise for large values of  $m_{t\bar{t}}$ , we choose to conduct this analysis by using events with  $m_{t\bar{t}} > 1 \text{ TeV}/c^2$ .

This analysis is a simple counting experiment, utilizing the total number of events which have  $m_{t\bar{t}} > 1 \text{ TeV}/c^2$ . We use the same QCD multijet background determined from data, and the SM  $t\bar{t}$  background determined from Monte Carlo. The counting experiment assumes that the efficiency of any new physics is the same as the efficiency for that of SM  $t\bar{t}$  production. We measure the efficiency of SM  $t\bar{t}$  events with  $m_{t\bar{t}} > 1 \text{ TeV}$  to be  $3.44 \pm 1.72 \times 10^{-4}$  for type 1+1 events. The uncertainty includes the same 50% uncertainty applied to the shape analysis. We assume the same 50% uncertainty on the signal efficiency.

We proceed to count the number of events with  $m_{t\bar{t}} > 1 \text{ TeV}/c^2$ . Table 10 shows the observed number of data events, along with the background expectation in this analysis.

The reconstructed mass of the  $t\bar{t}$  system is corrected to generator-level with bin-by-bin Monte Carlo corrections. The generator-level correction is  $24.8\% \pm 3.5\%$  for the  $m_{t\bar{t}} > 1.0 \text{ TeV}/c^2$  point in the “type 1 + 1” analysis. Figure 36 shows the reconstructed versus generated  $t\bar{t}$  masses for the “type 1 + 1” analysis. The same procedure as in the top-pair differential cross section [28] is used to correct the reconstructed mass to the generated mass. The correction in each bin is

$$\epsilon_i = \frac{N_i^{rec}}{N_i^{gen}}. \quad (4)$$

This simultaneously unfolds and corrects for acceptance effects.

With these numbers in hand, we proceed to perform the counting experiment to set limits

Process	Type 1+1
SM $t\bar{t}$	$486.6 \pm 243.3$
QCD Multijet	$4295 \pm 301$
Total Background	$4782 \pm 387$
Observed Data	4645
$t\bar{t}$ Efficiency	$3.4 \pm 1.7 \cdot 10^{-4}$

Table 10: Expected numbers of background events and observed data events with  $m_{t\bar{t}} > 1$  TeV/ $c^2$ . Errors include the statistical contribution only.

on the strength of any possible enhancement in the  $m_{t\bar{t}}$  spectrum. This is done using a flat prior for the signal cross section, and log-normal priors for the nuisance parameters : the total background estimate, the luminosity, and the signal efficiency. The limit is expressed as a ratio to the SM  $t\bar{t}$  cross section for  $m_{t\bar{t}} > 1$  TeV/ $c^2$ :

$$\mathcal{S} = \frac{\int_{M_{t\bar{t}} > 1} \frac{d\sigma_{SM+NP}}{dM_{t\bar{t}}} dM_{t\bar{t}}}{\int_{M_{t\bar{t}} > 1} \frac{d\sigma_{SM}}{dM_{t\bar{t}}} dM_{t\bar{t}}}$$

In contrast to 2011, the 2012 analysis will now be using a Bayesian limit-setting technique, implemented with Markov Chain Monte Carlo (MCMC) for the Higgs group's statistical package [29]. To provide an apples-to-apples comparison, we have also run the 2011 limits with the same Bayesian formalism. The central value of the limit changes from 2.6 with the  $CL_S$  technique to 2.5 with the Bayesian.

The results that we obtain with the 2012 analysis are

$$\mathcal{S} < 1.72$$

with an expected value of 1.33 and credible intervals of 0.76–1.81 at 68% C.L. and 0.56–2.95 at 95% C.L. This is an improvement over the 7 TeV results, because the enhancement of the cross section from 7 to 8 TeV is more drastic in the high-mass tails. This also rules out almost all new physics interpretations of the forward-backward asymmetry anomaly at the Tevatron.

## 11 Conclusion

We have updated the search for new physics in the boosted all-hadronic  $t\bar{t}$  final state. We have studied the effect of the new 2012 running conditions on our top quark reconstruction algorithms, and do not observe a large dependence on the amount of pileup in the 2012 dataset. We follow a similar analysis strategy to that used in Ref. [10], using the same data-based QCD multijet estimation. With 11 fb $^{-1}$  of integrated luminosity, we exclude RS Gluons with masses up to 2.1 TeV/ $c^2$ , and exclude cross sections of 21 (59) fb, at the 95% CL, for a  $Z'$  model with a mass of 3 TeV and resonance width of 1% (10%).

## References

- [1] S. Dimopoulos and H. Georgi, "Softly Broken Supersymmetry and SU(5)", *Nucl. Phys.* **B193** (1981) 150, doi:10.1016/0550-3213(81)90522-8.
- [2] S. Weinberg, "Implications of Dynamical Symmetry Breaking", *Phys. Rev.* **D13** (1976) 974–996, doi:10.1103/PhysRevD.13.974.

- [3] L. Susskind, “Dynamics of Spontaneous Symmetry Breaking in the Weinberg- Salam Theory”, *Phys. Rev.* **D20** (1979) 2619–2625, doi:10.1103/PhysRevD.20.2619.
- [4] C. T. Hill and S. J. Parke, “Top production: Sensitivity to new physics”, *Phys. Rev.* **D49** (1994) 4454–4462, doi:10.1103/PhysRevD.49.4454, arXiv:hep-ph/9312324.
- [5] R. S. Chivukula, B. A. Dobrescu, H. Georgi et al., “Top quark seesaw theory of electroweak symmetry breaking”, *Phys. Rev.* **D59** (1999) 075003, doi:10.1103/PhysRevD.59.075003, arXiv:hep-ph/9809470.
- [6] N. Arkani-Hamed, A. G. Cohen, and H. Georgi, “Electroweak symmetry breaking from dimensional deconstruction”, *Phys. Lett.* **B513** (2001) 232–240, doi:10.1016/S0370-2693(01)00741-9, arXiv:hep-ph/0105239.
- [7] N. Arkani-Hamed, S. Dimopoulos, and G. R. Dvali, “The hierarchy problem and new dimensions at a millimeter”, *Phys. Lett.* **B429** (1998) 263–272, doi:10.1016/S0370-2693(98)00466-3, arXiv:hep-ph/9803315.
- [8] L. Randall and R. Sundrum, “A large mass hierarchy from a small extra dimension”, *Phys. Rev. Lett.* **83** (1999) 3370–3373, doi:10.1103/PhysRevLett.83.3370, arXiv:hep-ph/9905221.
- [9] L. Randall and R. Sundrum, “An alternative to compactification”, *Phys. Rev. Lett.* **83** (1999) 4690–4693, doi:10.1103/PhysRevLett.83.4690, arXiv:hep-th/9906064.
- [10] J. Conway, J. Dolen, R. Erbacher et al., “Search for BSM  $t\bar{t}$  Production in the Boosted All-Hadronic Final State”, CMS Note 2011/194, (2011).
- [11] CMS Collaboration, “Particle-Flow Event Reconstruction in CMS and Performance for Jets, Taus, and MET”, CMS PAS PFT-09-001 (2009).
- [12] M. Wobisch and T. Wengler, “Hadronization corrections to jet cross sections in deep-inelastic scattering”, arXiv:hep-ph/9907280.
- [13] Y. L. Dokshitzer, G. D. Leder, S. Moretti et al., “Better Jet Clustering Algorithms”, *JHEP* **08** (1997) 001, arXiv:hep-ph/9707323.
- [14] M. Cacciari, G. Salam, and G. Soyez, “FastJet 2.3 User Manual”, *Phys. Lett. B* **641** (2006).
- [15] CMS Collaboration, “A Cambridge-Aachen (C-A) based Jet Algorithm for boosted top-jet tagging”, CMS Physics Analysis Summary CMS-PAS-JME-009-01 (2009).
- [16] M. Cacciari, G. P. Salam, and G. Soyez, “The Catchment Area of Jets”, *JHEP* **04** (2008) 005, doi:10.1088/1126-6708/2008/04/005, arXiv:0802.1188.
- [17] M. Cacciari and G. P. Salam, “Pileup subtraction using jet areas”, *Phys. Lett.* **B659** (2008) 119–126, doi:10.1016/j.physletb.2007.09.077, arXiv:0707.1378.
- [18] CMS Collaboration, “Jet Energy Corrections determination at 7 TeV”, CMS PAS JME-10-010 (2010).
- [19] J. Group, “Jet Energy Corrections and Uncertainties. Detector Performance Plots for 2012.”.



- [20] CMS Collaboration, “Jet Performance in pp Collisions at  $\sqrt{s} = 7$  TeV”, *CMS PAS JME-10-003* (2010).
- [21] CMS Collaboration, “Study of Jet Substructure in pp Collisions at 7 TeV in CMS.”, *CMS Physics Analysis Summary CMS-PAS-JME-10-013*.
- [22] D. E. Kaplan, K. Rehermann, M. D. Schwartz et al., “Top Tagging: A Method for Identifying Boosted Hadronically Decaying Top Quarks”, *Phys.Rev.Lett.* **101** (2008) 142001, doi:10.1103/PhysRevLett.101.142001, arXiv:0806.0848.
- [23] S. D. Ellis, C. K. Vermilion, and J. R. Walsh, “Techniques for improved heavy particle searches with jet substructure”, *Phys.Rev.* **D80** (2009) 051501, doi:10.1103/PhysRevD.80.051501, arXiv:0903.5081.
- [24] S. D. Ellis, C. K. Vermilion, and J. R. Walsh, “Recombination Algorithms and Jet Substructure: Pruning as a Tool for Heavy Particle Searches”, *Phys.Rev.* **D81** (2010) 094023, doi:10.1103/PhysRevD.81.094023, arXiv:0912.0033.
- [25] J. M. Butterworth, A. R. Davison, M. Rubin et al., “Jet substructure as a new Higgs search channel at the LHC”, *Phys. Rev. Lett.* **100** (2008) 242001, doi:10.1103/PhysRevLett.100.242001, arXiv:0802.2470.
- [26] K. Agashe, A. Belyaev, T. Krupovnickas et al., “CERN LHC signals from warped extra dimensions”, *Phys. Rev. D* **77** (Jan, 2008) 015003, doi:10.1103/PhysRevD.77.015003.
- [27] T. Muller, J. Ott, and J. Wagner-Kuhr, “theta - a framework for template-based modeling and inference”, CMS Internal Note 2010/017, (2010).
- [28] CMS Collaboration, “Top pair differential cross sections”, *CMS PAS TOP-11-013* (2011).
- [29] G. Petrucciani, “Documentation of the RooStats-based statistics tools for Higgs PAG”, <https://twiki.cern.ch/twiki/bin/viewauth/CMS/SWGuideHiggsAnalysisCombinedLimit>.

## A Comparison of 2011 and 2012 datasets

In this analysis, we use the same methods and techniques used in the analysis of 2011 data. In this section, we compare distributions of jet quantities and jet substructure quantities used in the W and top tagging algorithms. Figure 37 shows these distributions for the leading jet, while Figure 38 shows the same distributions for the second jet. The distributions are shown for the jets used in the top tagging algorithm. The distributions are comparable between the 2011 and 2012 datasets.

We also study the jet kinematic and substructure distributions for the pruned jet collection used for the W tagging algorithm. These distributions are shown in Figure 39 and Figure 40 for the leading and sub-leading pruned jet, respectively.

## B 2012 Data Pileup Studies

The new conditions during the 2012 LHC run, most notably the decreased  $\beta^*$  parameter at the interaction point, leads to increase numbers of proton-proton interactions at each bunch crossing in the detector. This pileup effect can affect offline reconstruction, if not handled adequately. Figure 41 shows the difference in the pileup conditions between an early portion of

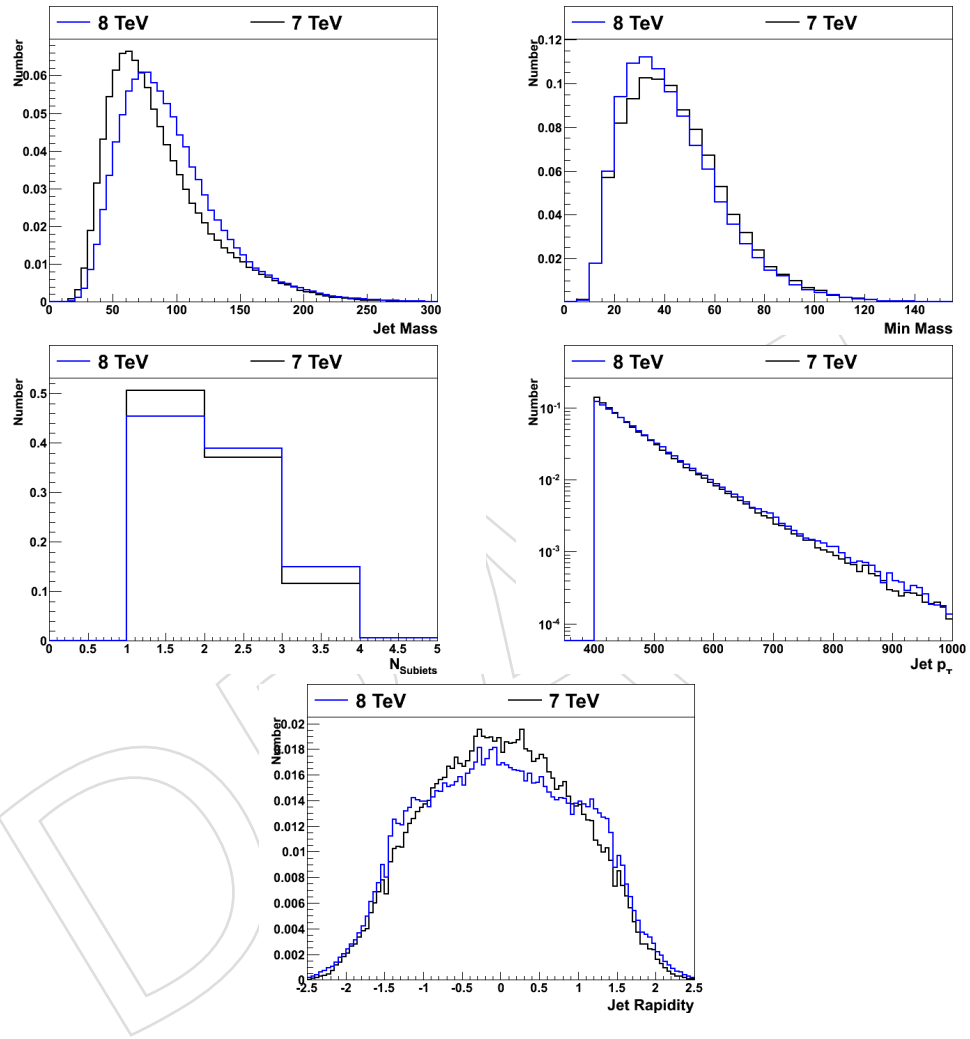


Figure 37: Comparisons of jet kinematic quantities for the leading jet in the top tagging jet collection



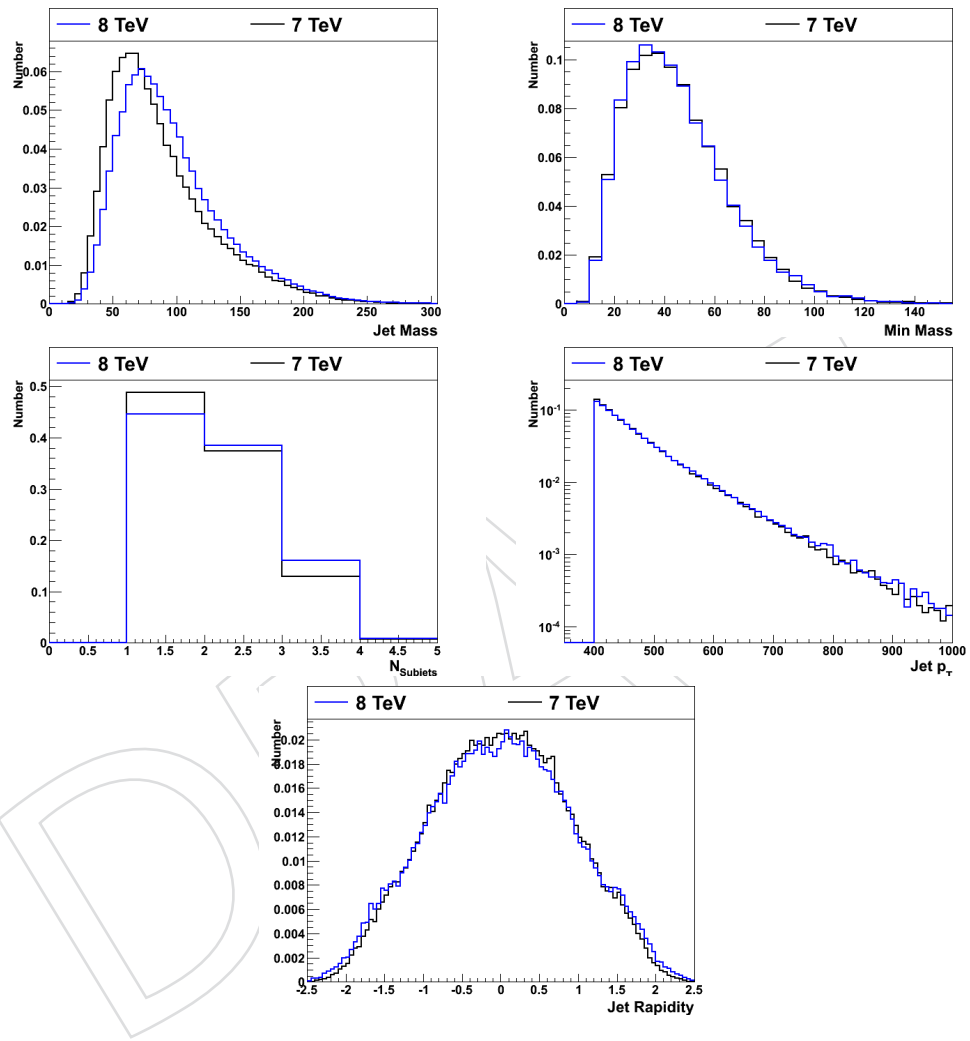


Figure 38: Comparisons of jet kinematic quantities for the second leading jet in the top tagging jet collection

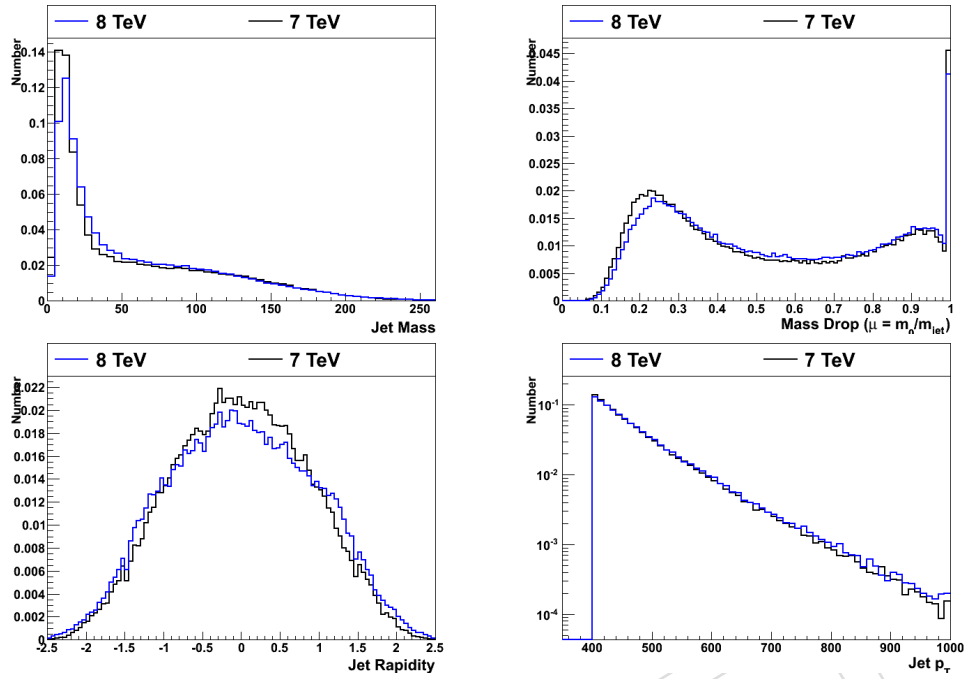


Figure 39: Comparisons of jet kinematic quantities for the leading jet in the pruned jet collection

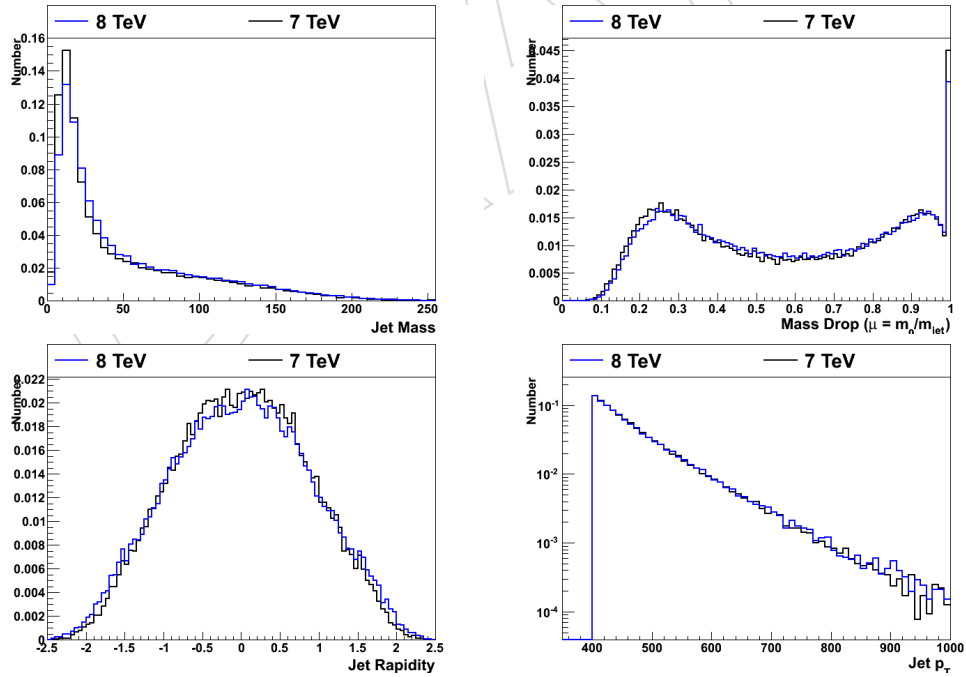


Figure 40: Comparisons of jet kinematic quantities for the second leading jet in the pruned jet collection

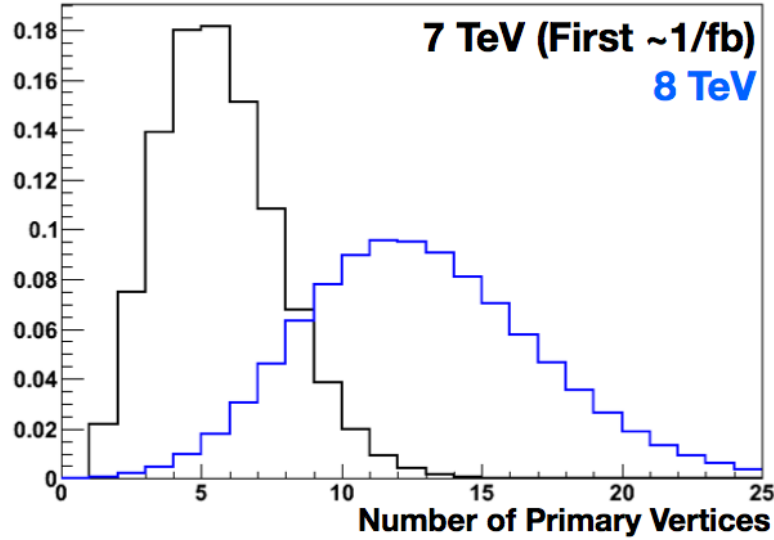


Figure 41: Number of reconstructed vertices for the early 2011 LHC run (black) and the 2012 run (blue).

the 2011 run and the 2012 run. The number of reconstructed vertices per event is much higher in the recent running. In this section, we demonstrate that the quantities used in the top and W tagging algorithms are relatively stable across differing numbers of reconstructed primary vertices in events.

Figure 42 shows two-dimensional plots of jet kinematic variables against the number of reconstructed primary vertices. Also drawn on the two-dimensional plots is a profile showing the mean value of the given distribution for each bin in the number of reconstructed vertices. This allows one to see the trend of various kinematic quantities with increasing numbers of reconstructed vertices. As can be seen from the plots, it appears the quantities used in the analysis are not strongly dependent on the number of vertices present in the event.

## C Luminosity Dependence of Trigger Selection

In the previous version of this analysis, the trigger PFJet320 was used. It was noticed that this trigger selection led to a deficit at low values of  $m_{t\bar{t}}$  in the type 1+2 topology. This effect can be seen in Figure 43. Due to this effect, it was decided to perform a study to determine if there existed any luminosity dependence due to the choice of trigger.

To perform this study, we use the selected type 1+2 events and the predicted type 1+2 events using the QCD mistag procedure outlined in the main text. We then compare the observation and prediction for various numbers of primary vertices. Figure 44 shows two-dimensional plots of  $m_{t\bar{t}}$  against the number of primary vertices in the event, for both the observed 1+2 events, and the events used to predict the QCD background in this channel.

We then take projections of these two-dimensional histograms, and look for a luminosity dependence. We use the ratio of the number of observed events to the number of predicted events, and plot this quantity as a function of the number of primary vertices in the event. This is shown in Figure 45, for the PFJet320 trigger. A linear fit is performed to quantify the luminosity dependence. The stack plot of this selection is shown, including the SM  $t\bar{t}$  expectation. We perform the same study using the new trigger selection, with HT750 instead of PFJet320. The

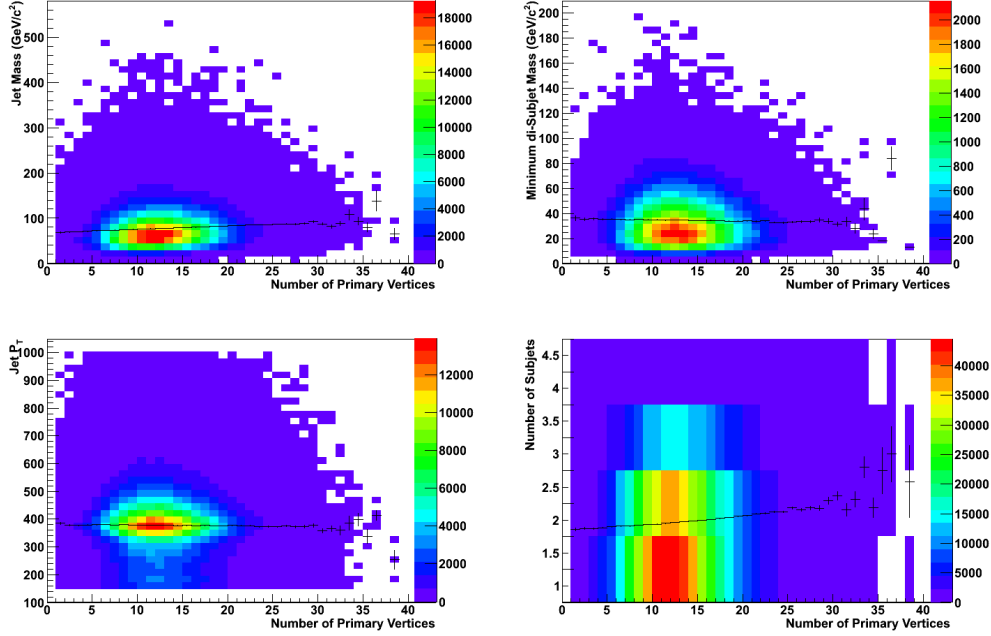


Figure 42: Two-dimensional plots of kinematic quantities versus the number of reconstructed primary vertices in the events. The black points are a profile histogram of the two-dimensional plot. The kinematic quantities do not depend strongly on the amount of pileup from additional vertices present in the event.

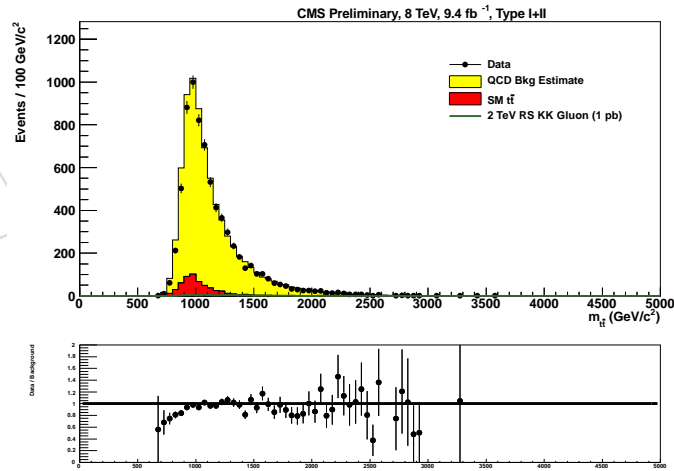


Figure 43: Result of the analysis of the type 1+2 topology, with the previous trigger selection: PFJet320. Note the deficit that appears at low values of  $m_{t\bar{t}}$ .

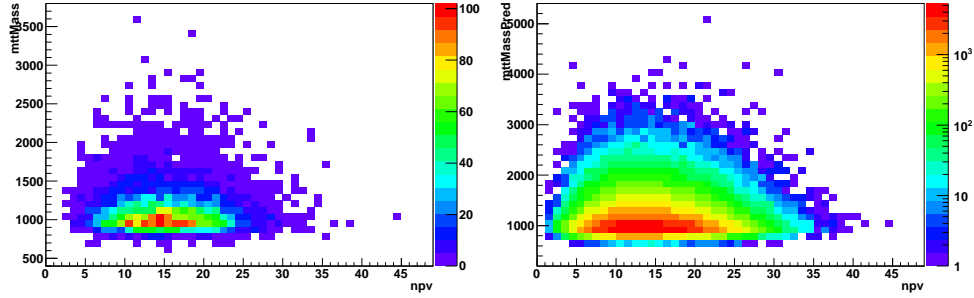


Figure 44: Plots showing the  $m_{t\bar{t}}$  distribution for different numbers of primary vertices in the event. The plot on the left shows events selected in the 1+2 topology, while the plot on the right shows the events used for the QCD prediction in the 1+2 channel.

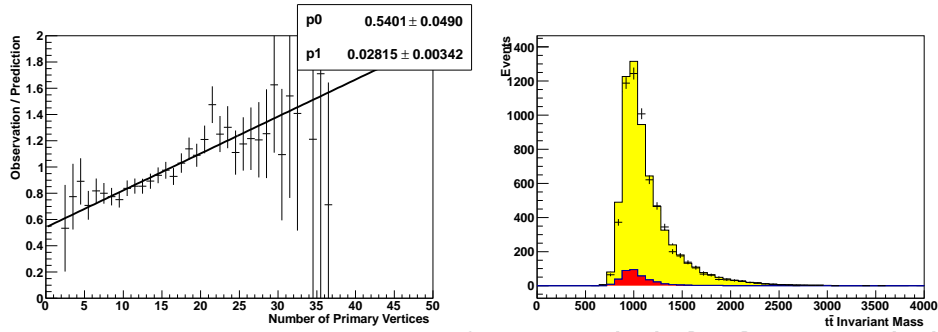


Figure 45: Pileup dependence of the ratio of observed events to predicted events, using the PFJet320 trigger selection. The deficit appears for low  $m_{t\bar{t}}$  with this trigger selection.

plots for this new trigger selection are shown in Figure 46. The agreement is much better with the HT750 trigger. The luminosity trend is still present, but is reduced by about 30% compared to the PFJet320 trigger selection.

We also check for this luminosity dependence using the QCD Monte Carlo samples with the trigger emulation applied. Figure 47 shows the result of this study using the HT750 trigger emulation on the QCD Monte Carlo samples. It can be seen that the luminosity trend exists also for the QCD Monte Carlo, but the closure test comparing observed and predicted events agrees quite well. The analogous plots are shown in Figure 48 with the PFJet320 trigger emulation applied.

As a final check, we also use the QCD Monte Carlo, but without any trigger selection or trigger emulation. It can be seen from Figure 49 that the same luminosity dependence exists in the absence of a trigger selection, but the agreement between the observation and prediction is still good.

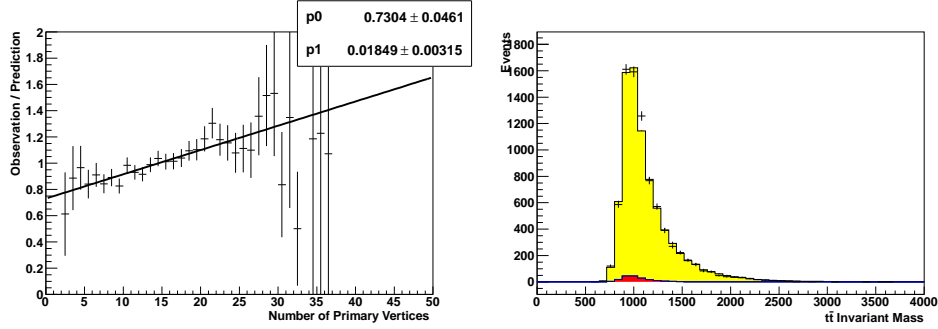


Figure 46: Pileup dependence of the ratio of observed events to predicted events, using the HT750 trigger selection. The agreement in the stack plot is much better with this trigger selection.

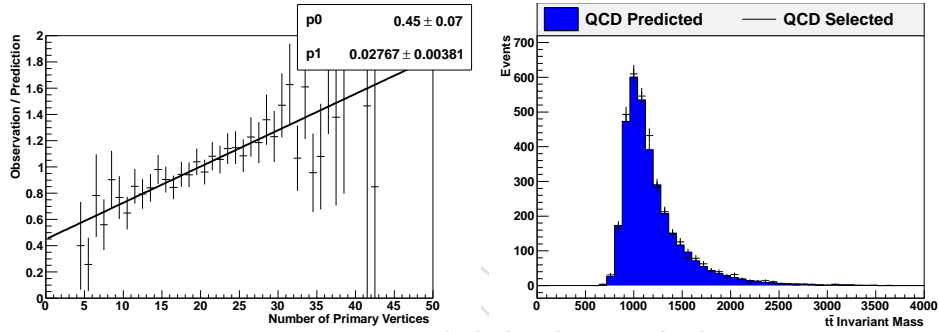


Figure 47: Pileup dependence of the ratio of observed events to predicted events, using the HT750 trigger selection applied to the QCD Monte Carlo samples. The right plot compares the selected QCD type 1+2 events (points) with the predicted distribution obtained from the mistag procedure outlined in the main text. The agreement is good in this plot, but the luminosity dependence still is present.

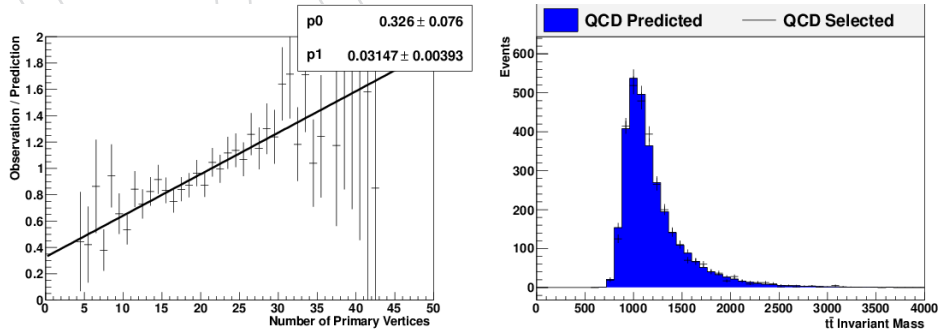


Figure 48: Pileup dependence of the ratio of observed events to predicted events, using the PFJet320 trigger selection applied to the QCD Monte Carlo samples. The right plot compares the selected QCD type 1+2 events (points) with the predicted distribution obtained from the mistag procedure outlined in the main text. The agreement is good in this plot, but the luminosity dependence still is present.

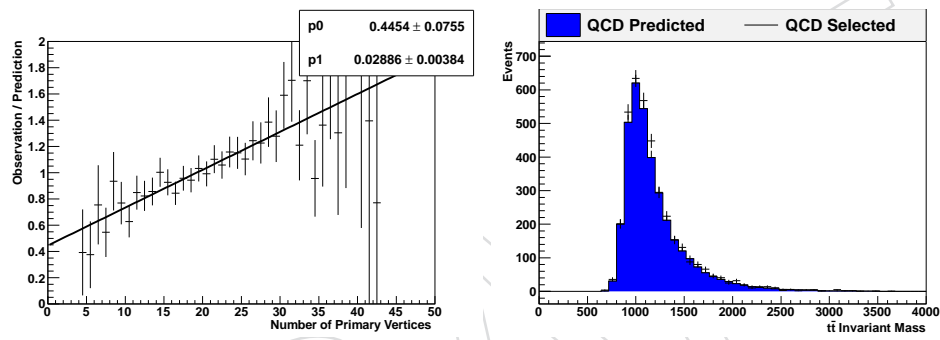


Figure 49: Pileup dependence of the ratio of observed events to predicted events, with no trigger selection applied to the QCD Monte Carlo samples. The right plot compares the selected QCD type 1+2 events (points) with the predicted distribution obtained from the mistag procedure outlined in the main text. The agreement is good in this plot, but the luminosity dependence still is present.